PAPER • **OPEN ACCESS**

Energy partitioning in N_2 microwave discharges: integrated Fokker–Planck approach to vibrational kinetics and comparison with experiments

To cite this article: M Altin *et al* 2022 *Plasma Sources Sci. Technol.* **31** 104003

OPEN ACCESS
IOP Publishing
Plasma Sources Science and Technology
Plasma Sources Sci. Technol. **31** (2022) 104003 (18pp)
https://doi.org/10.1088/1361-6595/ac93af

Energy partitioning in N_2 microwave discharges: integrated Fokker–Planck approach to vibrational kinetics and comparison with experiments

M Altin[1], P Viegas[2,3], L Vialetto[4], A W van de Steeg[5], S Longo[6], G J van Rooij[1] and P Diomede[1,*]

[1] Faculty of Science and Engineering, Maastricht University, 6211 KH Maastricht, The Netherlands
[2] Department of Physical Electronics, Faculty of Science, Masaryk University, 611 37 Brno, Czech Republic
[3] Instituto de Plasmas e Fusão Nuclear, Instituto Superior Técnico, Universidade de Lisboa, 1049-001 Lisboa, Portugal
[4] Theoretical Electrical Engineering, Faculty of Engineering, Kiel University, Kaiserstraße 2, 24143 Kiel, Germany
[5] DIFFER—Dutch Institute for Fundamental Energy Research, 5612 AJ Eindhoven, The Netherlands
[6] Dipartimento di Chimica, Università degli Studi di Bari, 70126 Bari, Italy

E-mail: p.diomede@maastrichtuniversity.nl

Received 21 June 2022, revised 6 September 2022
Accepted for publication 21 September 2022
Published 17 October 2022

Abstract

This work investigates energy transfers between electrons, vibrational and translational degrees of freedom and their effect on dissociation mechanisms in a N_2 microwave plasma in the pressure range between 50 and 400 mbar. A novel self-consistent 0D plasma chemistry model describing vibrational kinetics via the vibrational energy equation and the Fokker–Planck approach is developed. It is used to simulate conditions achieved experimentally, providing good agreement with measured values of vibrational and gas temperature and electron density. Above 100 mbar, energy efficiency of dissociation increases with power density, due to the significant contribution of collisions between vibrationally excited N_2 and electronically excited molecules. Energy transfer to vibrations is maximum at low power density and low pressure due to reduced gas heating.

Keywords: microwave discharges, nitrogen, comparison of simulations with experiments, energy partitioning, Fokker–Planck approach to vibrational kinetics

(Some figures may appear in colour only in the online journal)

1. Introduction

Nitrogen based compounds, used mostly as fertilizers, are crucial for sustaining intensified agricultural practices and the food production chain [1]. The practical use of N_2 as raw material for these compounds is hindered by the stable $N \equiv N$ triple bond. Non-biological fixation of N to either hydrogen or oxygen to provide precursors to the synthesis of more complex molecules has been under study for optimization since the beginning of the 20th century [2, 3]. In particular, a lot of effort has been devoted to the study of low-temperature plasmas, as the high vibrational excitation that they can maintain facilitates the breaking of the triple bond by lowering the dissociation

* Author to whom any correspondence should be addressed.

energy barrier. In fact, studies on NO_x production in plasma discharges have correlated the reaction rate to vibrational excitation, as non-thermal reactions were shown to provide the most relevant contribution to radical production [4].

The effect of vibrational excitation on the dissociation rate has been suggested by Fridman [5], who showed theoretically an increased energy efficiency of the dissociation process with increasing vibrational and gas temperature of N_2. Values of energy cost per atom as low as 6.3 eV were reached for pressures below 10 Torr and vibrational temperature above 6000 K. A recent study on MW pulsed discharges with pure nitrogen has pointed at electron-impact dissociation of vibrationally excited N_2 as a major contribution to N production during the first half of the pulse, when relatively high electron temperatures are reached ($\sim$2 eV) and electron density is around 10^{20} cm^{-3} [6]. Other computational studies on nitrogen dissociation in plasma DC discharges have highlighted the importance of collisions between vibrationally excited N_2 and electronically excited states through:

$$N_2(X, v) + N_2(A) \rightarrow N_2(X, v = 0) + N + N$$

to explain experimentally measured N densities [7–9] at pressures up to $\sim$5 mbar. As shown in a recent study by Volynets *et al* [10], this reaction dominates N production at values of the reduced electric field below 50 Td and is taken over by electron driven dissociation for higher values. Regardless of the dominant channel, vibrational levels are involved in the dissociation process, leading to the possibility of reducing the energy cost per formed atom, if energy is efficiently loaded into vibrational degrees of freedom. This is not true for thermal dissociation, as the excess energy remains available to the system, so that efficiency is not changed, while kinetics is.

The fraction of energy provided to the vibrational manifold can be estimated through measurements of the vibrational temperature (T_v) and the number density of the first vibrational states, as performed by Gatti *et al* [11], who showed both high levels of vibrational excitation in the core of a continuous MW discharge and high degrees of non-equilibrium outside the core at pressures below 50 mbar. Further investigation on pulsed MW discharges has been carried out by Van Alphen *et al* [12], who showed promising levels of energy loading into vibrations at 25 mbar of operating pressure. To what extent those conditions may increase dissociation efficiency remains to be determined. A recent combined experimental and computational effort by van de Steeg *et al* [13] and Kelly *et al* [6] on a pulsed MW discharge at 25 mbar has pointed out that collisions with atomic nitrogen quench vibrations, therefore hinting at the fact that efficient dissociation could be detrimental to energy confinement in vibrational degrees of freedom.

The experimental measurement of the vibrational distribution function (VDF) fails for higher vibrational levels due to their relatively low population [11]. Since these are crucial to determine the effect of vibrational excitation on dissociation, simulations are required to determine their population. However, the description and modelling of the VDF is computationally expensive, as it adds 46 additional balance equations to the master equation. A technique theoretically developed in the 70s and 80s [14–17], allows to replace the 46 rate balance equations for vibrational levels with a single equation, known as Fokker–Planck (FP) equation, which describes the motion of particles in energy space due to different types of collisions through a diffusion and a drift coefficient. Though recently benchmarked for the vibrational kinetics of CO_2 [18–20] and extended for N_2 to include also multi-quanta transitions [21], the technique has never been coupled with a 0D self-consistent global model. In effect, the evolution in time of all species number densities, gas temperature, electron temperature and electron energy distribution function (EEDF) is described. Validation and optimization of this technique can prove useful for the development of fast higher dimensional models, which appear to be necessary to capture all aspects of MW discharges [10, 22, 23].

The chemistry set proposed recently by Guerra *et al* [24] has been extensively used in the past for simulating low pressure conditions (below $\sim$10 mbar), which is significantly below a typical MW discharge pressure and gas temperatures ($T_g < 1500$ K), leaving open questions about their scalability. Increase in operating pressure up to (near) atmospheric is motivated by the higher appeal for future applications and energy consumption abatement [4]. To the best of our knowledge, no combined experimental and computational study has been carried out in N_2 MW plasmas above 50 mbar.

In this work, a self-consistent 0D model for the core of a MW generated N_2 plasma is developed, coupling the FP approach to vibrational kinetics with the solution of the master equation for chemically reactive species, the heat equation, the vibrational energy balance equation and the electron Boltzmann equation. With the aim of discharge characterization and model validation, *in situ* optical techniques have been used to measure gas, vibrational and electron temperature, and electron density in the core of a MW generated N_2 plasma at pressures between 50 and 400 mbar, and varying input powers. Mechanisms of energy transport between different degrees of freedom and their effect on dissociation are then investigated. With respect to Gatti's work [11], the addition of the measurements of electron temperature and density is motivated by the important role played by electrons in dissociation, already pointed out above.

This paper is organized as follows. Section 2 contains an overview of the experimental set-up and the investigated conditions. Section 3 describes the 0D self-consistent global model, with details on the implementation of the FP approach to vibrational kinetics. The comparison between simulated and measured temperatures and electron density is shown in subsection 4.1, while subsections 4.2 and 4.3 illustrate insight into both energy exchanges and dissociation.

2. Experimental set-up

The experimental setup is schematically shown in figure 1. Plasma is generated in a cylindrical quartz tube (27 mm outer diameter and 200 mm length) by continuous microwave radiation (2.45 GHz) delivered by a cavity magnetron with adjustable power and carried by a rectangular waveguide. Impedance matching with the plasma load is obtained using an

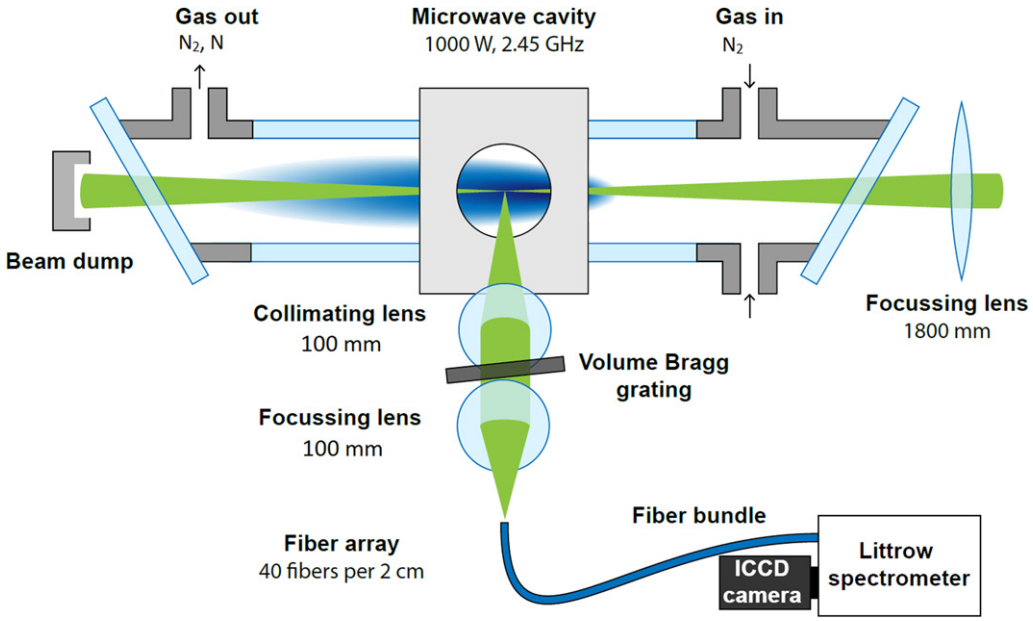

Figure 1. Schematic of the experimental set-up, detailed in the text. The collection optics shown is the one used for Thomson scattering measurements. Reprinted with permission from [26] © The Optical Society. Reprinted with permission from[27]. Copyright (2022) American Chemical Society. The collection optics for Raman scattering measurements is described in the text.

E–H tuner, which can be regulated to minimize the reflected power. The tangential injection of the input gas by means of two injection nozzles positioned 10 cm upstream of the waveguide, allows the formation of a swirl that stabilizes the plasma. More details on the setup can be found in previous works [13, 25].

The diagnostics is provided by a 30 Hz frequency doubled Nd:YAG laser ($\lambda = 532$ nm) of 400 mJ focussed on the axis of the tube. The light scattered by the plasma is collected perpendicular to the beam. The collection optics for Raman spectroscopy consists in a $f = 75$ mm lens focussing the scattered light into a fibre bundle; stray light and Rayleigh light are filtered out using a 532 nm long pass filter positioned in front of the fibre array. For Thomson scattering measurements, light is collimated by a $f = 100$ mm lens onto a Bragg grating, which reflects the scattered Rayleigh light [27]; the light transmitted by the grating is focussed into the fibre bundle by a $f = 100$ mm lens. Further reduction of stray light is obtained by a closing aperture positioned in front of the fibres. The light collected by the fibres is projected into a custom built Littrow spectrometer, equipped with an iCCD camera.

Thomson scattering is employed to calculate electron density n_e, which is proportional to the intensity of the scattered signal, and temperature T_e, which is proportional to its width [13, 28, 29]. N_2 rotational Raman spectrum at room temperature and 50 mbar of pressure was used as calibration, necessary to obtain an absolute value for electron density.

Vibrational and rotational temperatures (T_v and T_g) are measured through Raman scattering, as already successfully shown in recent works [11–13]. Raman scattered photons experience either gain or loss of a discrete amount of energy, caused by the de-excitation or excitation, respectively, of the scatterer (N_2 molecules in this case) from the ro-vibrational state (v, J) to (v', J'). In particular, the Q-branch ($\Delta J = J' - J = 0$) of the Stokes ($\Delta v = v' - v = 1$) Raman emission of N_2 molecules is considered in this work, as it provides the most intense signal. For a given initial vibrational level v, the intensity of the Stokes Q-branch peak is given by [11]:

$$I_v \propto \gamma_v(\tilde{\nu}_L - \Delta\tilde{\nu})^4 n_{v,J} \tag{1}$$

where γ_v is the polarizability of the molecule in the vibrational state v and is calculated as $\gamma_v = \gamma_0(v+1)$, where γ_0 is a constant for a given molecule. The fitting technique is described in detail in Gatti *et al* [11]. The experimental vibrational temperature is calculated using the population of the ground (n_0) and the first (n_1) vibrational levels, through:

$$T_v = \frac{\epsilon_{10}}{\ln(n_0/n_1)}. \tag{2}$$

Where ϵ_{10} is the energy difference between the first vibrational level and the vibrational ground state. In order to fit experimental data previous works have used an additional vibrational temperature (T_{15}), calculated assuming that the vibrational levels from 1 to 5 are populated according to a Boltzmann distribution with temperature T_{15}. Since only steady state conditions are investigated in this work, T_{15} is not considered relevant for the analysis.

Plasma imaging has been employed to obtain an indication of the size of the plasma [12, 13]. The emission intensity has been fitted assuming a Gaussian profile both in the radial and in the axial direction:

$$I(r, z=0) = a_r \exp\left(-\frac{r^2}{\sigma_r^2}\right) \tag{3}$$

$$I(r=0, z) = a_z \exp\left(-\frac{z^2}{\sigma_z^2}\right). \tag{4}$$

Table 1. Overview of experimental conditions and estimated peak input power density $P_{d,0}$ and measured T_v and T_g in the core.

P_{in} (W)	p (mbar)	r_p (mm)	L (mm)	$P_{d,0}$ (W cm^{-3})	$T_v/10^3$ (K)	$T_g/10^3$ (K)
300	50	4.8	36.7	75	5.9 ± 0.4	4.2 ± 0.2
300	100	3.4	26.6	207	6.6 ± 0.4	7.7 ± 0.5
300	200	2.2	18.8	677	6.7 ± 0.5	7.4 ± 0.9
300	400	1.9	16.8	1051	7.2 ± 0.2	6.0 ± 0.4
600	50	5.6	37.8	107	5.7 ± 0.3	4.6 ± 0.7
600	100	3.7	33.4	277	6.5 ± 0.5	7.3 ± 0.6
600	200	2.5	31.8	617	7.6 ± 0.6	9.1 ± 0.8
600	400	2.4	33.1	627	8.1 ± 0.5	8.3 ± 0.6
800	50	5.9	40.3	119	6.0 ± 0.9	4.6 ± 0.4
800	100	3.6	34.9	357	7.0 ± 0.5	8.4 ± 0.9
800	200	2.8	37.8	579	8.7 ± 0.6	8.6 ± 0.9
800	400	2.6	40.2	611	8.9 ± 0.5	9.0 ± 1.0

The input power density has been assumed to follow the same profile as the optical emission intensity:

$$P_d(r,z) = P_{d,0}\,\exp\left(-\frac{r^2}{\sigma_r^2}\right)\exp\left(-\frac{z^2}{\sigma_z^2}\right) \tag{5}$$

where the peak power density, $P_{d,0}$, is calculated imposing:

$$P_{\text{in}} = \int_{-\infty}^{+\infty} \mathrm{d}z \int_0^{2\pi} \mathrm{d}\theta \int_0^{R_{\text{tube}}} P_d(r,z) r\,\mathrm{d}r \tag{6}$$

R_{tube} is the radius of the quartz tube and P_{in} is the input power (W). Note that a more precise profile can be obtained including also a dependence of σ_r on z, since the plasma radial width decreases as $|z - z_0|$ increases. However, this additional detail does not provide significant variations in the calculated peak power density. Moreover, instead of the peak power density, the average value of P_d in the plasma core has been calculated, yielding, for every condition, a value that is about $0.6P_{d,0}$. This value is considered to be within the large uncertainties in input power density (estimated to be $\pm 50\%$ of the calculated value [30]) associated with the use of equation (5). These uncertainties are due to both the assumption that the power density profile is directly proportional to the emission intensity and the fact that part of the power is reflected and not absorbed [23].

Plasma radius r_p and length L shown in table 1 are calculated as the full width at half maximum of the light emission intensity profile and will be used to calculate transport properties in the global model. At $P_{\text{in}} = 300$ W, both the radius and the length of the plasma core decrease significantly with pressure, leading to an increase in the input power density. At higher input powers, r_p behaves similarly to the 300 W case, while L experiences a slower decrease, and at times even at slight increase with pressure. Since $P_{d,0}$ depends on $\sigma_r^{-2}\sigma_L^{-1}$, this causes the power density to saturate at 200 and 400 mbar. This contraction behaviour is similar to what already observed for CO_2 [22, 30], although less pronounced.

3. Self-consistent 0D plasma chemistry model

The experimental conditions listed in table 1 are simulated using a 0D time-resolved global model, considering only the plasma core [30]. This model includes N_2(X), the ground electronic state of molecular nitrogen, resolving all of its vibrational levels, electronically excited states of N_2 (N_2(A), N_2(B), N_2(C), N_2(a), N_2(a′), N_2(w)), atomic nitrogen in its ground state (N(S)) and two electronically excited states (N(D) and N(P)), the ionic species N_2^+, N^+, N_4^+ and N_3^+, and electrons (e). The model employs the kinetic scheme recently proposed by Guerra *et al* [24]: the reactions are explicitly listed in tables 2–5. Gas temperature, electron mean energy and vibrational temperature evolve self-consistently according to their energy balance equations, which are detailed in the following. Diffusive transport in both radial and axial direction and convective transport due to the input flux of particles are treated by means of characteristic times, also detailed in the following.

3.1. Vibrational kinetics

45 vibrational levels of N_2(X) are considered, as extensively used in literature [6, 31] and recommended by Guerra *et al* [24]. The vibrational kinetics scheme is detailed in table 2. The temporal evolution of the VDF is described using a FP equation, a method recently benchmarked against the widely used state-to-state (STS) method for CO_2 by Viegas *et al* [20] and for N_2 in [21]. Through the FP approach, the temporal evolution of the VDF is described as:

$$\frac{\mathrm{d}f(\epsilon)}{\mathrm{d}t} = -\frac{\mathrm{d}}{\mathrm{d}\epsilon}\left[A(\epsilon)f(\epsilon) - B(\epsilon)\frac{\mathrm{d}f(\epsilon)}{\mathrm{d}\epsilon}\right] + S_{\text{e-V}}(\epsilon) + S_{\text{V-T},mq}(\epsilon) + S_{\text{chem}}(\epsilon) - \frac{f(\epsilon)}{\tau_c} \tag{7}$$

where $f(\epsilon)$ is the particle density per unit of energy and ϵ is the vibrational energy. The first term in equation (7) contains the drift ($A(\epsilon)$) and diffusion ($B(\epsilon)$) coefficients in the vibrational energy space, used to model monoquantum vibrational–vibrational (V–V) and vibrational–translational (V–T) processes; their form and derivation will be presented in another paper [21]. $S_{\text{eV}}(\epsilon)$ is a source/sink term containing the contributions from electron impact vibrational excitations (e–V) and de-excitation processes, $S_{\text{V-T},mq}(\epsilon)$ accounts for V–T collisions involving exchanges of more than one quantum of energy, $S_{\text{chem}}(\epsilon)$ accounts for interactions between N_2(X) vibrational levels and other heavy species in the model; those terms are calculated as:

$$S(\epsilon) = \sum_p k_p(\epsilon')n_p f(\epsilon') - \sum_q k_q(\epsilon)n_q f(\epsilon) \tag{8}$$

where indexes p and q run over all processes causing either the creation or the destruction, respectively, of a molecule at vibrational energy ϵ, $n_{p,q}$ are the number densities of the collision partners and $k_{p,q}$ are the rate coefficients.

The last term on the right-hand side of equation (7) describes losses or gains of particles due to convective transport, with the characteristic time τ_c defined by equation (18).

Table 2. Processes for vibrational kinetics, included in the FP model. Rate coefficients are discussed in the text. Processes involving other species (*Chemistry*), can be found in tables 3 and 4.

Process name	Reaction
e–V	$e + N_2(v = n) \leftrightarrow e + N_2(v = m)$; $n = 0{:}45$, $0 < (m - n) \leqslant 10$
$V–V_1$	$N_2(v = n) + N_2(v = 1) \leftrightarrow N_2(v = n + 1) + N_2(v = 0)$
$V–V_2$	$N_2(v = n) + N_2(v = 2) \leftrightarrow N_2(v = n + 1) + N_2(v = 1)$
$V–V_n$	$N_2(v = n) + N_2(v = n) \leftrightarrow N_2(v = n + 1) + N_2(v = n - 1)$
V–T	$N_2(v = n) + M \leftrightarrow N_2(v = n - 1) + M$
	$N_2(v = n) + N \leftrightarrow N_2(v = m) + N$, $\max[0, n - 5] \leqslant m < n$, $n > 6$
e–D	$e + N_2(v) \rightarrow e + N + N$
V–D	$N_2(v = 45) + N_2(v = 1) \rightarrow N + N + N_2(v = 0)$
	$N_2(v = 45) + N_2(v = 45) \rightarrow N + N + N_2(v = 44)$
	$N_2(v = n) + N_2(v = m) \rightarrow N + N + N_2(v = 0)$, $10 \leqslant n, m \leqslant 25$
	$N_2(v = 45) + N_2 \rightarrow N + N + N_2$
	$N_2(v) + N \rightarrow N + N + N$
Chemistry	See tables 3 and 4

Table 3. List of heavy particle reactions [24]. Rate coefficients units are $m^3\ s^{-1}$ for two-body collisions, $m^6\ s^{-1}$ for three-body collisions and s^{-1} for radiative transitions. T_g is expressed in K.

	Reaction	Rate coefficient
(N1)	$N_2(A) + N_2(A) \rightarrow N_2(C) + N_2(X, v = 2)$	1.5×10^{-16}
(N2)	$N_2(A) + N_2(A) \rightarrow N_2(B) + N_2(X, v = 8)$	7.7×10^{-17}
(N3)	$N_2(A) + N_2(X, v = 5{:}14) \rightarrow N_2(B) + N_2(X, v = 0)$	2×10^{-17}
(N4)	$N_2(w) + N_2(X) \rightarrow N_2(a) + N_2(X)$	1×10^{-17}
(N5)	$N_2(a) + N_2(X) \rightarrow N_2(a') + N_2(X)$	2×10^{-17}
(N6)	$N_2(a') + N_2(X) \rightarrow N_2(B) + N_2(X)$	1.9×10^{-19}
(N7)	$N_2(B) + N_2(X) \rightarrow N_2(A) + N_2(X)$	$0.95 \times 3 \times 10^{-17}$
(N8)	$N_2(B) + N_2(X) \rightarrow N_2(X, v = 0) + N_2(X)$	$0.05 \times 3 \times 10^{-17}$
(N9)	$N_2(B) + N_2(B) \rightarrow N_2(B) + N_2(X, v = 9)$	3.6×10^{-16}
(N10)	$N(P) + N(S) \rightarrow N(S) + N(S)$	1.8×10^{-18}
(N11)	$N(P) + N(S) \rightarrow N(D) + N(S)$	6×10^{-19}
(N12)	$N(D) + N_2(X) \rightarrow N(S) + N_2(X)$	$1 \times 10^{-19} \exp(-510/T_g)$
(N13)	$N(P) + N_2(X) \rightarrow N(S) + N_2(X)$	6×10^{-20}
(N14–N17)	$N_2(A) + N(S) \rightarrow N_2(X, v = 6{:}9) + N(P)$	1×10^{-17}
(N18)	$N_2(X, v = 39{:}v_{max}) + N(S) \rightarrow N_2(A) + N(D)$	1×10^{-17}
(N19)	$N_2(X, v = 38{:}v_{max}) + N(S) \rightarrow N_2(a') + N(S)$	1×10^{-18}
(N20)	$N_2(X, v = 10{:}v_{max}) + N(P) \rightarrow N_2(A) + N(S)$	$1 \times 10^{-16} \exp(-1300/T_g)$
(N21)	$N_2(X, v = 15{:}19) + N_2(A) \rightarrow N_2(X, v = 0) + N(S) + N(S)$	$4.5 \times 10^{-17} \exp(-1765/T_g)$
(N22)	$N(S) + N(S) + N_2(X) \rightarrow N_2(B) + N_2(X)$	$8.27 \times 10^{-46} \exp(500/T_g)$
(N23)	$N_2(C) \rightarrow N_2(B) + h\nu$	2.74×10^{7}
(N24)	$N_2(B) \rightarrow N_2(A) + h\nu$	2.0×10^{5}
(N25)	$N_2(a) \rightarrow N_2(X, v = 0) + h\nu$	1.8×10^{4}
(N26)	$N_2(a) \rightarrow N_2(a') + h\nu$	1.91×10^{2}
(N27)	$N_2(w) \rightarrow N_2(a) + h\nu$	6.5×10^{2}

The population of vibrationally excited states ($n(\epsilon)$) in units of m^{-3} is retrieved using [20]:

$$n(\epsilon) = \int \delta(\epsilon - \epsilon') f(\epsilon') \mathrm{d}\epsilon' \tag{9}$$

where $\delta(\epsilon - \epsilon')$ is the Dirac delta function.

At the right boundary of the energy domain (ϵ_{diss}), an outflux of particles is caused by dissociation mechanisms. The dissociation flux is calculated considering all processes causing the exchange of a single quantum of energy:

$$J_{diss} = n(\epsilon_{diss}) \big[k_{V-V1}(\epsilon_{diss}) n_1 + k_{V-V_n}(\epsilon_{diss}) n(\epsilon_{diss}) + k^r_{V-T}(\epsilon_{diss}) n_{N_2} + k^r_{V-T(N)}(\epsilon_{diss}) n_{max} \big] \tag{10}$$

where the superscript r identifies a reverse reaction, n_1 is the number density of the first vibrationally excited state and n_{max} is the number density of the topmost vibrational state. Note that dissociation processes taking place due to the exchange of more than one quantum are included, instead, in the term $S_{chem}(\epsilon)$.

Table 4. List of charged particles reactions [24]. Rate coefficients units are $m^3\ s^{-1}$ for two-body collisions and $m^6\ s^{-1}$ for three-body collisions. v_{max} is considered to be 45. T_e and T_g are expressed in K.

	Reaction	Rate coefficient
(I1)	$N_2(a') + N_2(a') \rightarrow e + N_4^+$	5×10^{-17}
(I2)	$N_2(A) + N_2(a') \rightarrow e + N_4^+$	1×10^{-17}
(I3)	$N_2(a') + N(P) \rightarrow e + N_3^+$	1×10^{-17}
(I4)	$N(D) + N(P) \rightarrow e + N_2^+(X)$	1×10^{-19}
(I5)	$N_2^+(X) + N_2(X, v = 12{:}v_{max}) \rightarrow N_2^+(B) + N_2(X, v' = v - 12)$	1×10^{-17}
(I6)	$N_2^+(X) + N_2(X, v = 0) + N_2(X) \rightarrow N_4^+ + N_2(X)$	$6.8 \times 10^{-41}(300/T_g)^{1.64}$
(I7)	$N_2^+(X) + N(S) + N_2(X) \rightarrow N_3^+ + N_2(X)$	$9 \times 10^{-42} \exp(400/T_g)$
(I8)	$N^+ + N_2(X, v = 0) + N_2(X) \rightarrow N_3^+ + N_2(X)$	$1.7 \times 10^{-41}(300/T_g)^{2.1}$
(I9)	$N_4^+ + N_2(X) \rightarrow N_2^+(X) + N_2(X, v = 0)\ N_2(X)$	$2.1 \times 10^{-22} \exp(T_g/121)$
(I10)	$N_3^+ + N(S) \rightarrow N_2^+(X) + N_2(X, v = 0)$	6.6×10^{-17}
(I11)	$e + N_2^+(X) \rightarrow N(D) + N(D)$	$2.8 \times 10^{-13}\sqrt{300/T_e}$
(I12)	$e + N_2^+(X) \rightarrow N(S) + N(D)$	$2 \times 10^{-13}\sqrt{300/T_e}$
(I13)	$e + N_4^+ \rightarrow N_2(X, v = 0) + N_2(X, v = 0)$	$2 \times 10^{-12}\sqrt{300/T_e}$
(I14)	$e + N_3^+ \rightarrow N_2(X, v = 0) + N(S)$	$2 \times 10^{-13}\sqrt{300/T_e}$
(I15)	$N_2^+(B) \rightarrow N_2^+(X) + h\nu$	1.6×10^7

Table 5. Reactions describing the electron kinetics.

	Reaction	Reference
(E1)	$e + N_2(v = n) \leftrightarrow e + N_2(v = m);\ n = 0\text{–}45,\ 0 < (m - n) \leqslant 10$	[24, 37]
(E2)	$e + N_2(X, v) \leftrightarrow e + N_2(A, B, C, a, a', w)$	[37]
(E3)	$e + N_2(A) \leftrightarrow e + N_2(B, C)$	[38]
(E4)	$e + N_2(B) \leftrightarrow e + N_2(C)$	[38]
(E5)	$e + N_2(a) \leftrightarrow e + N_2(a', w)$	[38]
(E6)	$e + N_2(a') \leftrightarrow e + N_2(w)$	[38]
(E7)	$e + N(S) \leftrightarrow e + N(P, D)$	[39]
(E8)	$e + N(P) \leftrightarrow e + N(D)$	[39]
(E9)	$e + N_2^+(X) \rightarrow e + N_2^+(B)$	[37]
(E10)	$e + N_2(X, A, B, a, a') \rightarrow e + e + N_2^+(X)$	[38]
(E11)	$e + N_2(X) \rightarrow e + e + N_2^+(B)$	[37]
(E12)	$e + N(S, D, P) \rightarrow e + e + N^+$	[39]
(E13)	$e + N_2(v) \rightarrow e + N(S) + N(S, D)$	[37, 40]

To ensure that the VDF has the right normalization, the total population of the electronic ground state $N_2(X)$ is calculated at every time step from the previous iteration as:

$$n_{N_2(X)}(t) = n_{N_2(X)}(t - \Delta t) + \left[\int_0^{\epsilon_{diss}} \left(S_{chem}(\epsilon) - \frac{f(\epsilon)}{\tau_c}\right) d\epsilon + \frac{\sum_i m_i n_i}{m_{N_2}\tau_c} - J_{diss}\right]\Delta t \quad (11)$$

and the populations of all vibrational levels are then normalized to that value.

The temporal evolution of the mean vibrational energy ($\langle\epsilon_v\rangle$) is described by the vibrational energy balance equation:

$$\frac{d\langle\epsilon_v\rangle}{dt} = \sum_p \omega_p \frac{n_{v,p}}{n_{N_2(X)}}\Delta E_p - \sum_{v=1}^{45} \frac{\epsilon_v - \epsilon_{v-1}}{\tau_{N_2(X),d}} - \sum_{v=1}^{45} \frac{\epsilon_v}{\tau_c} \quad (12)$$

where ω_p is the frequency of process p, ΔE_p is the energy exchange involved in the process, $n_{v,p}$ is the population of the vibrational level v involved in the collision p, $n_{N_2(X)}$ is the number density of nitrogen molecules in the electronic ground states and ϵ_v is the vibrational energy of level v. The first term describes the vibrational energy lost or gained per unit time through collisions with other molecules, the second term describes the energy lost per unit time due to vibrational deactivation at the wall (with $\tau_{N_2(X),d}$ defined in equation (20)) and the last term describes the energy loss per unit time due to convective transport in the axial direction. At every iteration, the vibrational temperature is evaluated from $\langle\epsilon_v\rangle$ by inverting equations (3)–(194) in [5]:

$$\langle\epsilon_v\rangle(T_v) = \frac{\hbar\omega_e}{e^{(\hbar\omega_e/T_v)} - 1} \quad (13)$$

with ω_e being the characteristic vibrational frequency of N_2, taken as 2358.57 cm^{-1} [31, 32]. The population of the ground vibrational level and the first excited one are then constrained so that equation (2) holds.

The rate coefficients for V–V_1, V–V_2, V–V_n and V–T (see table 2 for an explanation of these acronyms) collisions are calculated following the work by Adamovich *et al* [32, 33] and Ahn *et al* [34], where they are derived according to the forced harmonic oscillator (FHO) theory, which provides

very good agreement with quantum classical trajectory (QCT) calculations [35] even at higher temperature and is therefore preferred for the simulations of high temperature plasmas [36]. In contrast, the parametrization presented by Guerra *et al* [24], based on first-order perturbation theory, is not suitable for high collision energies and deviates from semiclassical calculations [35] for temperatures above 1000 K.

Note that a limited set of V–V collisions is considered. First of all, only monoquantum energy exchanges are considered, as they are the most likely [31]. Secondly, only resonant ($V–V_n$) and two non-resonant processes are considered ($V–V_1$ and $V–V_2$). The choice of considering only $V–V_2$ is justified by the fact that for any other $V–V_i$ process to be relevant, it is necessary that the ratio between its rate coefficient and the rate coefficient for $V–V_1$ is greater than or approximately equal to the ratio n_1/n_i. At lower gas temperatures (<1000 K), this ratio is high enough to justify the inclusion of additional V–V collisions. However, at the values of T_g listed in table 1, this condition may hold only in the case of extreme non-equilibrium, which is not observed in the present study.

3.2. Chemical and charged particles kinetics

The temporal evolution of all species number densities, except for the vibrational levels of $N_2(X)$ and electrons, is described by their volume averaged rate equations:

$$\frac{\mathrm{d}n_i}{\mathrm{d}t} = S_{i,\mathrm{vib}} + S_{i,\mathrm{chem}} - \frac{n_i}{\tau_{i,d}} - \frac{n_i}{\tau_c} \tag{14}$$

where n_i is the number density of species i, $S_{i,\mathrm{vib}}$ and $S_{i,\mathrm{chem}}$ are terms accounting for creation or destruction of species i due to reactions with vibrationally excited $N_2(X)$ or with any other species, respectively; $\tau_{i,d}$ and τ_c are the characteristic times for diffusive and convective transport, respectively, and they are defined in equations (20) and (18).

For the atomic nitrogen species N(S), an additional term due to dissociation from the last vibrational state of $N_2(X)$ is added and has the form $2J_{\mathrm{diss}}$. The source term $S_{i,\mathrm{vib}}$ takes into account the coupling with the vibrational kinetics and is calculated by considering the population of vibrational states, from the solution of the FP equation, as fixed; its contribution to the population of species i is calculated as:

$$S_{i,\mathrm{vib}} = \sum_v n(\epsilon_v) k_{v,j} n_j - \sum_v n(\epsilon_v) k_{i,v} n_i \tag{15}$$

where v, the vibrational quantum number, runs over all vibrational levels involved in either the creation (first summation) or the destruction (second summation) of species i, $n(\epsilon_v)$ is the population (in m^{-3}) of vibrational level v, as obtained from the solution of the FP equation, $k_{j,v}$ is the rate coefficient of the reaction having species j and $N_2(X, v)$ as reactants and n_j is the number density of the collision partner. Note that in some cases, for example the V–V dissociation of $N_2(X)$, creating N(S), both reactants are vibrationally excited nitrogen molecules, hence n_j is substituted by $n(\epsilon_{v'})$, where v' is the vibrational quantum number of the collision partner. The processes included in the chemistry set are extensively described in a recent review by Guerra *et al* [24] and explicitly listed in tables 3 and 4.

3.3. Electron kinetics

In order to maintain quasi-neutrality in the plasma, the electron number density, rather than obeying its own rate equation, is calculated as:

$$n_e = \sum_i n_i \ \mathrm{sgn}(q_i) \tag{16}$$

where i runs over all ionic species, q_i is the charge of the ion and sgn is the sign function. Instead, electron mean energy (ϵ_e) evolves in time as [20]:

$$\frac{\mathrm{d}(n_e\epsilon_e)}{\mathrm{d}t} = P_{d,0}(t) - \frac{P_{\mathrm{el}}}{n_{\mathrm{gas}}}(\epsilon_e) n_{\mathrm{gas}} n_e - \frac{P_{\mathrm{inel}}}{n_{\mathrm{gas}}}(\epsilon_e) n_{\mathrm{gas}} n_e - \frac{n_e\epsilon_e}{\tau_{e,d}} - \frac{n_e\epsilon_e}{\tau_c} \tag{17}$$

where n_e is the electron density, $P_{d,0}$ is the peak input power density, derived from experiments, $P_{\mathrm{el}}(\epsilon_e)$ is the power lost through elastic collisions, $P_{\mathrm{inel}}(\epsilon_e)$ is the power lost through inelastic collisions, including also energy gains from superelastic processes, and the last two terms account for the energy losses due to transport, with $\tau_{e,d}$ and τ_c being characteristic times for diffusion and convection, respectively, which are defined in equations (20) and (18). The implementation of equation (17) is preferred over the local field approximation, as this allows one to take into account electron energy losses due to transport, therefore avoiding overestimation of the electron mean energy, as pointed out by previous works [41, 42].

The rate coefficients for electron-impact collisions are tabulated as a function of mean electron energy by solving the electron Boltzmann equation for different values of input reduced electric field (E/n_{gas}). As the electron mean energy evolves according to equation (17), rate coefficients are calculated by linear interpolation between the tabulated values. The electron-impact processes considered in this work and the references for their cross sections are listed in table 5. All reactions cross sections are included in the electron Boltzmann solver (BOLSIG+), while their calculated rate coefficients are included in the global model.

3.4. Transport

Axial convective transport is accounted for by assuming that all species formed inside the core leave after a characteristic residence time, defined as:

$$\tau_c = \frac{L}{v} \tag{18}$$

where L is the length of the plasma, obtained from experiments, and v is the average gas speed, calculated using mass conservation under the assumption that all species have the same speed:

$$v = \frac{m_{\mathrm{N_2}} N_{\mathrm{in}} \Gamma_{\mathrm{in}}}{\sum_i m_i n_i A_{\mathrm{tube}}} \tag{19}$$

where $m_{\mathrm{N_2}}$ is the mass of the nitrogen molecule, N_{in} is the mass density of the input gas ($N_2(X, v = 0)$) at pressure p and

Table 6. Recombination and deactivation reactions due to transport towards the wall of neutral species. The rate for deactivation or recombination at the wall is calculated as $\tau_{i,d}^{-1}$. Details about the value of $\tau_{i,d}$ are discussed in the text.

	Reaction
(NT1)	$N_2(A) + \text{wall} \rightarrow N_2(X, v = 0)$
(NT2)	$N_2(B) + \text{wall} \rightarrow N_2(X, v = 0)$
(NT3)	$N_2(C) + \text{wall} \rightarrow N_2(X, v = 0)$
(NT4)	$N_2(a) + \text{wall} \rightarrow N_2(X, v = 0)$
(NT5)	$N_2(a') + \text{wall} \rightarrow N_2(X, v = 0)$
(NT6)	$N(S) + \text{wall} \rightarrow 0.5N_2(X, v = 0)$
(NT7)	$N(D) + \text{wall} \rightarrow \{N(S), 0.5N_2(X, v = 0)\}$
(NT8)	$N(P) + \text{wall} \rightarrow \{N(S), 0.5N_2(X, v = 0)\}$
(NT9)	$N_2(X, v) + \text{wall} \rightarrow N_2(X, v - 1)$

Table 7. Recombination reactions due to transport towards the wall of charged species. The rate for deactivation or recombination at the wall is calculated as $\tau_{i,d}^{-1}$. Details about the value of $\tau_{i,d}$ are discussed in the text.

	Reaction
(IT1)	$N_4^+ + \text{wall} \rightarrow 2N_2(X, v = 0)$
(IT2)	$N_3^+ + \text{wall} \rightarrow N_2(X, v = 0) + N(S)$
(IT3)	$N_2^+(X) + \text{wall} \rightarrow N_2(X, v = 0)$
(IT4)	$N_2^+(B) + \text{wall} \rightarrow N_2(X, v = 0)$
(IT5)	$N^+ + \text{wall} \rightarrow N(S)$

temperature 300 K, Γ_{in} is the input flux rate (in units $\text{m}^{-3}\ \text{s}^{-1}$), m_i and n_i are, respectively, the mass and the number density of species i and A_{tube} is the section area of the tube. Since it is assumed that the only species entering the core due to transport is $N_2(X, v = 0)$, for the vibrational ground state ($\epsilon \in [\epsilon_0, \epsilon_1[$), the FP equation (equation (7)) contains an additional term $+\frac{\sum_i m_i n_i}{m_{N_2}\tau_c}$.

In this work, particles of species i diffusing towards the wall undergo deactivation or recombination (for neutral species and charged heavy species, respectively) with probability γ_i. The characteristic time for losses due to diffusion in cylindrical geometry is calculated as [24]:

$$\tau_{i,d} = \frac{1}{D_i}\left[\left(\frac{J_0}{R}\right)^2 + \left(\frac{\pi}{L}\right)^2\right]^{-1} + \frac{\frac{2LR}{L+R}\left(1 - \frac{\gamma_i}{2}\right)}{\gamma_i \langle v_i \rangle} \tag{20}$$

where J_0 is the first zero of the zero order Bessel function and its value is approximately 2.405, R is the radius of the plasma core (table 1), $\langle v_i \rangle$ is the thermal velocity of species i and D_i is the diffusion coefficient of species i, calculated as [43]:

$$D_i = \frac{1 - y_i}{\sum_{j \neq i} x_j / D_{i,j}} \tag{21}$$

where y_i is the mass fraction of species i, x_j is the mole fraction of species j (with $j \neq i$) and $D_{i,j}$ is the binary diffusion coefficient for species i in species j. The latter is calculated as indicated by Guerra *et al* [24] (equation (37) in the paper) and it depends on Lennard-Jones binary interaction potential parameters [44]. Tables 6 and 7 contain all the included reactions; the deactivation probability for metastable states (listed in table 6) is assumed to be 1, recombination of N(S) at the wall is assumed to have probability 10^{-3} [31] and a 0.5 branching ratio is assumed for recombination or deactivation of excited states of N at the wall. Note that the creation of $N_2(X, v = 0)$ due to the deactivation of electronically excited species and recombination of ions and atomic nitrogen is contained in the source term denoted as $S_{\text{chem}}(\epsilon)$. The deactivation of vibrationally excited molecules involving only the loss of one quantum of energy, is treated within the FP approximation by defining a drift and diffusion coefficient in energy space [20]:

$$A_{\text{wall}}(\epsilon) = -\Delta E \frac{1}{\tau_d(\epsilon)} - \frac{\mathrm{d}B_{\text{V-T}}(\epsilon)}{\mathrm{d}\epsilon} \tag{22}$$

$$B_{\text{wall}}(\epsilon) = \frac{1}{2}\Delta E^2 \frac{1}{\tau_d(\epsilon)} \tag{23}$$

where the function $\tau_d(\epsilon)$ is the characteristic diffusion time as a function of vibrational energy ϵ and it is obtained through polynomial interpolation of the values of $\tau_{i,d}$ calculated with equation (20) for discrete vibrational levels. Note that different vibrational levels have different characteristic diffusion times, as the deactivation probability γ_v (with v vibrational quantum number), is assumed to depend linearly on v ($\gamma_v = \gamma_1 v$), with $\gamma_1 = 1.1 \times 10^{-3}$ [45, 46].

The diffusive transport of charged species is described by ambipolar diffusion. The ambipolar diffusion coefficient in a multicomponent gas is calculated as indicated by Guerra *et al* [31]:

$$D_{i,a} = D_i - \mu_i \frac{\sum_j n_j D_j}{\sum_j n_j \mu_j} \tag{24}$$

where index j runs over all charged species, including electrons, D_i (D_j) is the free diffusion coefficient of species i (j), μ_i (μ_j) is the mobility, taken negative for electrons, and n_i (n_j) is the number density of the charged species i (j). The free diffusion coefficients for ionic species in nitrogen as a function of the reduced electric field are derived, using the Einstein relation, from the ion mobility and tabulated by Ellis *et al* [47], while the electron mobility is calculated via BOLSIG+ [48]. The characteristic time for the diffusion of charged particles is therefore calculated using equation (20) with $D_{i,a}$ instead of D_i. It is assumed that all ions recombine at the wall with probability 1 [24].

3.5. Gas heating

Gas temperature is determined self-consistently by solving the heat equation, assuming a parabolic radial profile for the gas temperature in the tube [49, 50]:

$$c_p(T_g) n_m \frac{\mathrm{d}T_g}{\mathrm{d}t} = Q_{\text{in}} - Q_{\text{axial}} - Q_{\text{rad}} - \frac{8\lambda(T_g)}{R_{\text{tube}}^2}(T_g - T_{w,\text{in}}) \tag{25}$$

where c_p is the molar heat capacity of the gas, taken from the NIST database [51], n_m is the molar density of the gas, T_g is the radially averaged gas temperature, $\lambda(T_g)$ is the thermal conductivity of the mixture [52], R_{tube} is the radius of the tube, $T_{w,\text{in}}$ is the temperature of the inner wall. The last term on the right-hand side describes the heat loss to the wall. The thermal conductivity $\lambda(T_g)$ is calculated considering the contributions

of N and N_2, without distinguishing their excited states. Given the limited concentration of atomic nitrogen, $\lambda(T_g)$ is mainly determined by N_2 thermal conductivity.

The temperature next to the inner wall is calculated as suggested by Booth *et al* [53]:

$$T_{w,\text{in}} \approx T_w + 0.28(T_g - T_w) \tag{26}$$

where T_w is the temperature of the outer wall, assumed to be constant at 300 K; this relation was derived from measurements in a pure O_2 plasmas and, though it might be slightly different for pure N_2, it provides an approximate way of evaluating the decrease in heat flux to the wall due to the increase of its temperature [24].

All terms denoted by Q, account for losses or gains of translational energy per unit time and unit volume, due to different processes, detailed in the following.

Q_{in} is the power per unit volume exchanged between heavy particles or electrons and background gas molecules, calculated as:

$$Q_{\text{in}} = Q_{\text{V-V}} + Q_{\text{V-T}} + Q_{\text{chem}} + Q_{\text{wall}} + \frac{P_{\text{el}}}{n_{\text{gas}}}(\epsilon_e) n_e n_{\text{gas}} \tag{27}$$

where $Q_{\text{V-V}}$ and $Q_{\text{V-T}}$ are due to vibrational kinetics; their form is detailed in the works by Pintassilgo *et al* [50, 54]. The last term in Q_{in} takes into account elastic collisions with electrons and has already been introduced in equation (17). Q_{chem} contains heat exchanges due to chemical reactions, calculated as:

$$Q_{\text{chem}} = \sum_p k_p n_{p,1} n_{p,2} \Delta H_p. \tag{28}$$

The sum runs over all exothermic processes p, listed in table 8, k_p is the rate coefficient of the reaction, $n_{p,1}$ and $n_{p,2}$ are number densities of the two collision partners and ΔH_p is the energy released by the reaction. All the pooling reactions included in table 8 are summarized by Shkurenkov *et al* [55]; pooling reactions involving electronically excited states not considered in the present work have been discarded. Values of ΔH used in the present work differ slightly from the ones from the work by Shkurenkov *et al* [55] in some cases discussed in the following.

Since reactions N1 and N2, as taken from Guerra *et al* [24], lead to the formation of nitrogen molecules in the vibrational states $v = 2$ and $v = 8$, respectively, instead of $v = 4$ and $v = 12$, as assumed by Shkurenkov *et al* [55], the available energy for gas heating has been taken from Guerra *et al* [31].

Moreover, self-quenching of N_2(B) (N9) has been included, as suggested in a recent work by Lepikhin *et al* [56]. The fraction of energy made available for gas heating by reaction N7 is subject of discussion in literature, with Shkurenkov *et al* suggesting that only 70% (0.86 eV) is transferred to translational degrees of freedom, while the remainder is used for vibrational excitation of N_2(X) [55]; for pressures between 1 and 10 Torr, Pintassilgo *et al* [50] have shown that this choice produces only a limited change in gas temperature. Since no details about vibrational excitation of N_2(X) through reaction N7 are provided, for consistency the present work considers that no energy is transferred to vibrational degrees of freedom, leaving the total 1.18 eV available for gas heating.

In addition, reactions I11 and I12 have been added to the scheme proposed by Shkurenkov *et al* [55], as suggested by Lepikhin *et al* [56]. Note that previous works by Pintassilgo *et al* [49, 50], include the same reaction, producing N(S) + N(S) and having an available energy of 5.82 eV; however, since that reaction is not listed in the most recent review by Guerra *et al* [24] and is discarded by other works [56, 57], it has not been included in our model. Electron impact dissociation with the formation of N(S) + N(D) (last reaction in table 8) has also been added, as suggested by Pintassilgo *et al* [50]. It is however worth noticing that the same work states that the last three reactions in table 8 become relevant at values of the reduced electric field above 200 Td, which is almost one order of magnitude higher than what is expected in the experimental conditions of table 1.

Lastly, Q_{wall} in equation (27) is the contribution to gas heating due to deactivation of vibrationally excited states of N_2(X) and electronically excited states of N_2 and N at the wall. It is calculated as:

$$Q_{\text{wall}} = \sum_i \frac{n_i}{\tau_{i,d}} \Delta H_i \tag{29}$$

where i runs over all species of table 6 and all vibrationally excited states of N_2(X) and ΔH_i is the energy of excited species (for electronically excited molecules or atoms) or the single quantum energy jump in the case of vibrational deactivation.

Q_{axial} is the power per unit volume lost due to transport in the axial direction, and is calculated as:

$$Q_{\text{axial}} = \frac{1}{\tau_c}[n_m c_p(T_g) T_g - n_{m,\text{in}} c_p(T_{\text{bg}}) T_{\text{bg}}] \tag{30}$$

where T_{bg} is the background temperature (300 K) and $n_{m,\text{in}}$ is the molar density of the particles entering the core due to the input flux.

Q_{rad} is the heat loss due to radiation and is calculated as:

$$Q_{\text{rad}} = 4\pi\epsilon_{\text{N}} \tag{31}$$

where ϵ_{N} is the net emission coefficient, taken from the work of Aubrecht *et al* [58].

3.6. Numerical implementation of the model

The quantities used as input are the input power density P_d, the pressure p, the mass flow rate Γ_{in}, the length of the plasma L and the radius of the plasma core R. As initial condition, electron and N_2^+(X) number densities are set at 10^{14} m^{-3}, electron mean energy is set at 0.1 eV and the number density of all neutral species is assumed to be 0, except for the ground vibrational state of N_2(X), whose population is assumed equal to n_{gas}.

The FP equation used to describe vibrational kinetics is discretized on a 1000 cells grid in the vibrational energy space using a finite volume technique [21, 59]. The resulting tridiagonal matrix is inverted employing Thomas algorithm. The total number of control volumes is chosen so that the cell width is much smaller than the energy jumps. The master equation for all other species and the energy balance equation for electrons,

Table 8. All reactions included as contributions to gas heating. ΔH is the energy transferred to translational degrees of freedom, defined as enthalpy change in the reaction.

	Reaction	ΔH (eV)	Reference
(N1)	$N_2(A) + N_2(A) \rightarrow N_2(C) + N_2(X, v = 2)$	0.4	[31]
(N2)	$N_2(A) + N_2(A) \rightarrow N_2(B) + N_2(X, v = 8)$	2.0	[31]
(N3)	$N_2(A) + N_2(X, v = 5{:}14) \rightarrow N_2(B) + N_2(X, v = 0)$	0.24–2.54	[55]
(N4)	$N_2(w) + N_2(X) \rightarrow N_2(a) + N_2(X)$	0.34	[55]
(N5)	$N_2(a) + N_2(X) \rightarrow N_2(a') + N_2(X)$	0.15	[55]
(N6)	$N_2(a') + N_2(X) \rightarrow N_2(B) + N_2(X)$	0.24	[55]
(N7)	$N_2(B) + N_2(X) \rightarrow N_2(A) + N_2(X)$	1.18	[50]
(N8)	$N_2(B) + N_2(X) \rightarrow N_2(X) + N_2(X)$	7.35	[6]
(N9)	$N_2(B) + N_2(B) \rightarrow N_2(B) + N_2(X, v = 9)$	5.0	[56]
(N10)	$N(P) + N(S) \rightarrow N(S) + N(S)$	3.58	[55]
(N11)	$N(P) + N(S) \rightarrow N(D) + N(S)$	1.2	[24]
(N12)	$N(D) + N_2(X) \rightarrow N(S) + N_2(X)$	2.38	[54]
(N13)	$N(P) + N_2(X) \rightarrow N(S) + N_2(X)$	3.58	[54]
(N14–N17)	$N_2(A) + N(S) \rightarrow N_2(X, v = 6{:}9) + N(P)$	0.91–0.12	[55]
(N22)	$N(S) + N(S) + N_2(X) \rightarrow N_2(B) + N_2(X)$	2.44	[55]
(I11)	$e + N_2^+(X) \rightarrow N(D) + N(D)$	1.06	[56]
(I12)	$e + N_2^+(X) \rightarrow N(D) + N(S)$	3.44	[56]
(E13)	$e + N_2 \rightarrow e + N(D) + N(S)$	1.0	[50]

is solved numerically using a Runge–Kutta solver of order 5 (RADAU5). The heat equation and the vibrational energy balance equation are solved using a forward Euler algorithm.

The electron Boltzmann equation is solved employing BOLSIG+; due to the dependence of the EEDF on the composition of the gas, and in particular on the shape of the VDF [24], the solver is called every time a relevant change in the gas composition is detected. The condition that triggers the solver update is:

$$\begin{cases} \dfrac{n_i^1}{n_{\text{gas}}} > 0.1 \\ \Delta_1 = \max\limits_i \left[\dfrac{|n_i^1 - n_i^0|}{n_i^0} \right] > 0.1 \end{cases} \tag{32}$$

where n_i is the population of species i (including vibrationally excited states), superscript 0 indicates the population when the EEDF was last updated and 1 the one at the current time step. As already mentioned before, the electron Boltzmann equation is solved for different values of reduced electric field in order to retrieve a table with rate coefficients as a function of mean electron energy. Every time the Boltzmann solver is called (around 60 times per simulation), 5 different values of reduced electric field are considered: this number is chosen with the aim of not compromising the computational efficiency of the code. The explored interval is contained between $E_{\max}/n_{\text{gas}} = 1.5E_{\text{center}}/n_{\text{gas}}$ and $E_{\min}/n_{\text{gas}} = 0.8E_{\text{center}}/n_{\text{gas}}$, where $E_{\text{center}}/n_{\text{gas}}$ is calculated as:

$$\frac{E_{\text{center}}}{n_{\text{gas}}} = \frac{1}{n_{\text{gas}}} \sqrt{\frac{P_{d,0}}{2\mu_e n_e q_e}} \tag{33}$$

where μ_e is the electron mobility, obtained from the Boltzmann solver and q_e is the elementary charge. Note that the reduced electric field calculated with equation (33) is the average over a period of the MW power supply. The change in discharge composition and VDF is accounted for by changing the input composition for BOLSIG+, every time it is called (around 60 times per simulation).

After each time step, all populations are normalized to the total gas density in order to maintain isobaric conditions and the ideal gas law. At the end of each time step Δ_2 is calculated as:

$$\Delta_2 = \max_i \left[\frac{|n_i^1 - n_i^0|}{n_i^0} \right] \tag{34}$$

where i runs over all species, including vibrational levels, and indexes 0 and 1 indicate, respectively, the population at $t - dt$ and t, where dt is the time step, chosen adaptively and inversely proportional to Δ_2. When $\Delta_2 < 10^{-8}$, the steady state is considered to be reached and the simulation is ended.

The average computational time required to reach convergence depends on the specific simulated conditions, ranging from 30 to 50 min, with an average of 700 s to simulate 1 ms of physical time. Even though the calculation of A and B coefficients for the FP equation is the computationally most expensive step, the code still outperforms a STS code not implementing the FP approach for vibrational kinetics, which takes about 1000 s to simulate 1 ms of physical time.

4. Results

4.1. Comparison between simulations and experiments

Using as input the peak power densities listed in table 1, all 12 experimental conditions have been simulated, providing values of gas temperature, vibrational temperature, electron temperature and electron density which are compared to the experimental results in figures 2–5. For the sake of clarity, only selected results are shown: in particular, results obtained with 300 W and 600 W of input power are plotted as a function of pressure. The error bars associated to the simulated values, represented by the coloured shade in the pictures, are obtained

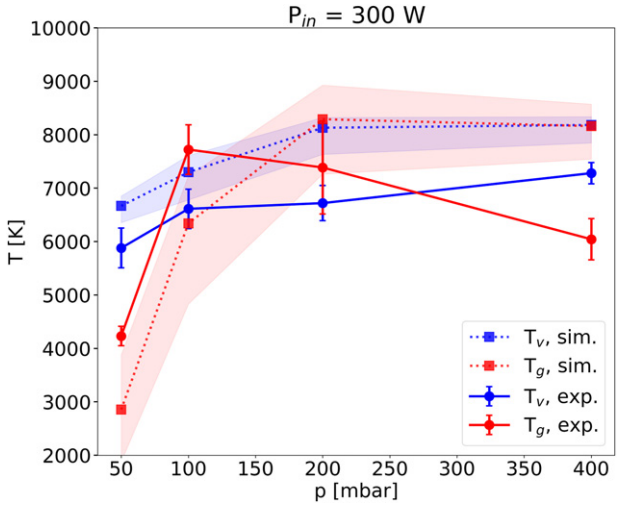

Figure 2. Gas and vibrational temperature as a function of pressure for $P_{\text{in}} = 300$ W, in the plasma core. The shaded area represents results obtained with a $\pm 50\%$ variation of input power density.

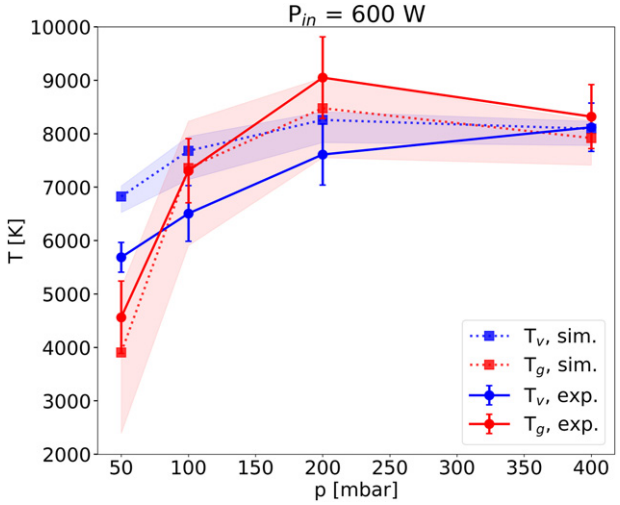

Figure 3. Gas and vibrational temperature as a function of pressure for $P_{\text{in}} = 600$ W, in the plasma core. The shaded area represents results obtained with a $\pm 50\%$ variation of input power density.

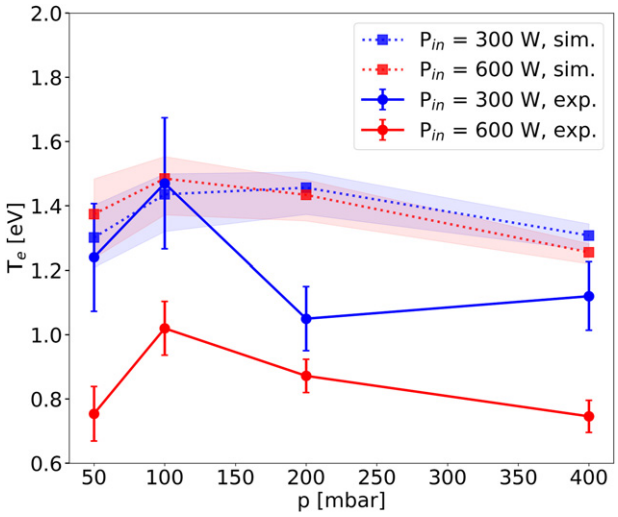

Figure 4. Electron temperature obtained from experiments and simulations as a function of pressure, at two different values of input power, in the plasma core.

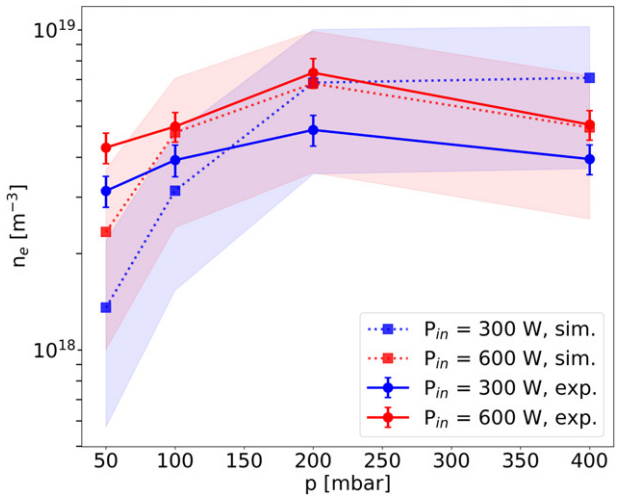

Figure 5. Electron density obtained from experiments and simulations as a function of pressure, at two different values of input power, in the plasma core.

by varying the input power density by $\pm 50\%$ and provide a quick estimation of the sensitivity of simulation results to uncertainties in the input parameters, as already discussed in the description of the experimental set-up.

Simulated gas temperature, as shown in figures 2 and 3, increases with pressure, since gas heating mechanisms, which involve V–T relaxation and quenching of electronically excited states, are strongly dependent on gas density; the main gas heating channels are investigated more in detail in the next subsection. As these mechanisms also strongly depend on the excitation of N_2, power density also plays an important role in determining T_g. In fact, as shown by the shaded regions in the plot, variations of roughly ± 1000 K are triggered by the change in $P_{d,0}$ at every simulated condition. The relative variation of T_g decreases from roughly $\pm 30\%$ at 50 mbar to $\pm 10\%$ at 400 mbar, suggesting that pressure is a limiting factor in gas heating above 100 mbar. The dependence of T_g on $P_{d,0}$ also explains why simulated results at 300 W and 600 W are very similar: for higher pressures, despite doubling the input power, the increase in core size as a function of input power limits the change in $P_{d,0}$ and thus the change in T_g.

According to experiments, electron density increases with increasing input power (figure 5), while electron temperature decreases. Though the increased n_e is not reproduced by simulations in some cases, this can be imputed to the strong dependence of electron density on $P_{d,0}$, as shown by the large error bars. Moreover, it is worth noting that the discrepancy in n_e at 300 W resembles the discrepancy in gas temperature which can be observed in figure 2, where simulations underestimate T_g by about 1000 K at 50 and 100 mbar and overestimate the one at 200 and 400 mbar. If the main source of gas heating comes from quenching of excited states, which are mostly created

through electron impact, the strong relation between n_e and T_g is explained. At 600 W, both experimental n_e and T_g are quantitatively well reproduced by the simulations.

Figures 2 and 3 also show the comparison between experimental and simulated vibrational temperatures, revealing a good qualitative agreement at both values of input power. In particular, T_v/T_g decreases as pressure is increased, due to increased V–T reaction rates. However, T_v appears to be slightly overestimated by simulations; as T_v is less sensitive to variations of $P_{d,0}$, this discrepancy can be caused by the overestimation of T_e, discussed below, or by an underestimation of the loss of vibrationally excited molecules due to transport, which is inevitably approximated in a 0D framework. It is also worth noting that, in some cases, experimental results show $T_g > T_v$, a condition which is also reproduced by simulations, particularly for cases at high $P_{d,0}$. This behaviour of the simulated T_g and T_v is due to the fact that equilibrium is established by V–T processes (which leads to $T_g = T_v$), dissociation, which depopulates the tail and therefore counters the tendency of T_v towards T_g and by reaction N3, which lowers vibrational temperature, heats the gas and is also the main channel for the creation of N_2(B). It should be noted that, as it will be clarified in the next subsections, quenching of N_2(B) provides a large part of the gas heating, therefore leading to further increase in T_g.

As shown in figure 4, electron temperature is, in most cases, overestimated by the model. Moreover, the variation in input power does not cause in the simulated results the variation suggested by the experimental ones: namely, a decrease in mean electron energy from 300 W to 600 W. As suggested by equation (17), electron temperature should depend directly on $P_{d,0}$, while depending inversely on n_e. The limited variation in T_e in simulations is thus explained by the counterbalancing effect of the increased n_e (figure 5) with the increase in input power density. It should also be noted that transport could play a role in the cooling of electron temperature, pointing at a shortcoming of the 0D model as a possible cause of the discrepancy.

In summary, comparison with experiments has revealed the main role played by input power density in determining gas temperature and electron density. A link between the two through electronic excitation has been highlighted and will be investigated in the following section. Vibrational temperature is consistently overestimated by simulations and is less sensitive to variations of power density, suggesting the presence of processes counterbalancing the increasing input power density, like transport or reactions like N3. The main shortcoming of the 0D model is in the description of transport. In fact, the sharp gradients of gas temperature and vibrational temperature, which vary from thousands of Kelvins in the core to almost room temperature near the wall, may induce increased losses, therefore reducing T_v in the core. The application of 1D models, taking into account mass and energy transport could provide a more accurate description of warm microwave discharges [22, 23].

4.2. Energy redistribution mechanisms

The MW power injected in the system and absorbed by electrons is spent to excite N_2 or N to electronic states other than the ground state, populate the vibrational manifold of N_2(X), ionize molecules and atoms and cause dissociation of N_2. The relative contribution of those mechanisms to the total rate of energy loss for electrons is shown in figure 6 for the 300 W case, as the 600 W and 800 W results show the same trend. Superelastic collisions causing the de-excitation of vibrationally or electronically excited N_2 or N are sources of energy for electrons: figure 6 only shows the net loss.

Most of the electron energy is redistributed to electronic and vibrational excitation; the relative contribution of the latter increases from 20 to 35% as pressure is increased from 50 to 200 mbar and decreases back to ∼20% at 400 mbar. This effect is due to a decrease in the reduced electric field from 200 (42 Td) to 400 mbar (35 Td).

Note that this trend in energy partition is in very good agreement with what is predicted by Guerra *et al* [24]. In that work, assuming a Treanor–Gordiets distribution at $T_v =$ 4000 K and $T_g = 300$ K, the dominant contribution to electron energy losses at a value of $E/n_{\text{gas}} \sim 30$ Td is shown to be vibrational excitation, while electronic excitation takes up ∼10% of the electron energy. The higher percentage shown in this work (∼30%) is due to the higher vibrational temperature reached in the discharge and the fact that superelastic collisions with electronically excited states are also considered. A recent study on pulsed MW discharges in pure N_2 by Kelly *et al* [6] at 25 mbar, shows a significantly higher contribution of electronic excitation towards the end of the pulse, even though the calculated value of E/n_{gas} is around 10 Td. This behaviour is due to both the higher concentration of N achieved during the first part of the pulse (where power density reaches ∼8 kW cm^{-3}) and the higher concentration of electronically excited states of N_2 which can populate the high energy tail of the EEDF via superelastic collisions.

Electron impact with N_2(X) is the most relevant source of vibrational excitation, while other reactions forming vibrationally excited molecules, like N1 and N2, can be neglected. The energy transferred from electrons to vibrational excitation can be lost through V–T relaxation, due to collisions with either molecular or atomic nitrogen, electronic excitation (reactions N3, N21, N22 and N23), dissociation or axial transport. Figure 7 shows the relative contribution of each process to the losses of vibrational energy: V–T relaxation due to collisions with N and dissociation are never relevant energy sinks, while V–T with N_2, electronic excitation (mainly reaction N3) and axial transport consume most of the energy stored in the vibrational manifold. As already highlighted in the previous subsection, the relevant contribution of both reaction N3 and axial transport to vibrational cooling can explain the weak dependence of T_v on input power density, as both counterbalance the increasing $P_{d,0}$. As T_g approaches T_v, V–T contribution tends to 0, since the VDF tends to a Boltzmann distribution, as shown in figure 12. The increased V–T heating rate at 100 mbar is due to the shape of the VDF (figure 12): though the first levels are populated as a Boltzmann

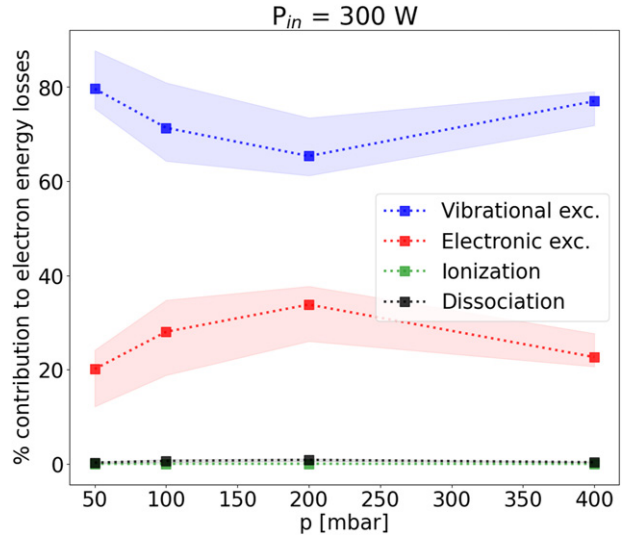

Figure 6. Relative contribution of different processes to electron energy losses obtained from simulations as a function of pressure, at $P_{\text{in}} = 300$ W.

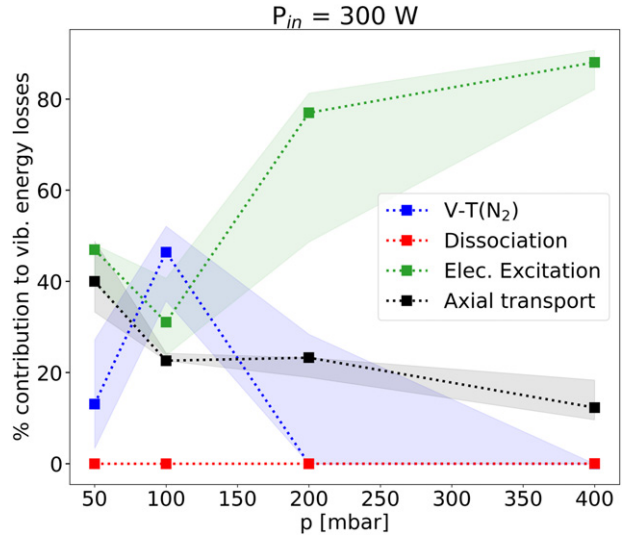

Figure 7. Relative contribution of different processes to vibrational energy losses obtained from simulations as a function of pressure, at $P_{\text{in}} = 300$ W.

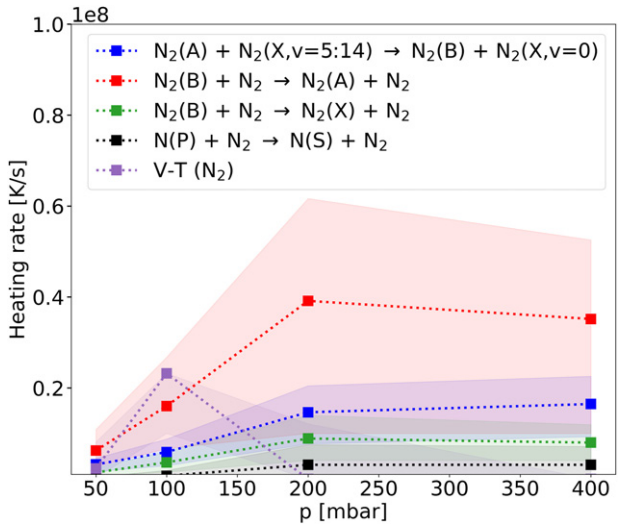

Figure 8. Heating rate for different processes obtained from simulations as a function of pressure, at $P_{\text{in}} = 300$ W.

distribution, the tail of the distribution is slightly overpopulated, allowing a net contribution from V–T collisions, whose rate coefficients are significantly higher than the ones for the 50 mbar case due to the higher T_g.

The energy transferred to translational degrees of freedom, causing heating of the gas, derives either from vibrations (as discussed above) or from other exothermic reactions, listed in table 8. The fraction of energy conveyed into gas heating was estimated as the ratio of the heat rate per unit volume over the input power density; in the investigated conditions, around 30% of input power density is used for gas heating. This value reflects the percentage of energy given to electronically excited states from collisions with electrons, due to the dominance of quenching of electronically excited states among the gas heating mechanisms. Figure 8 shows the relative contribution of the most relevant processes: most of the heating comes from quenching of electronically excited states. These species are mainly populated through electron collisions with N_2 in the ground state, hence higher electron density will result in an increased heating rate, leading to a higher gas temperature. The relevance of reaction N3 for both gas heating and vibrational cooling explains why T_g shows a higher sensitivity than T_v to $P_{d,0}$ variations, as can be seen in figures 2 and 3: in fact, increased $P_{d,0}$ and hence increased electron density, provides a higher density of N_2(A), which in turn increases the N3 reaction rate, countering the increase of vibrational temperature that would otherwise occur due to the increase in e–V reaction rates.

As the equilibrium between gas and vibrational temperature is obtained through V–T collisions, the low contribution of these processes both in gas heating and vibrational energy losses at 50 mbar justifies the higher degree of non-equilibrium observed at low pressure. In turn, V–T rate coefficients are kept low by the slowly increasing gas temperature, due to the lower density of N_2(A, B), whose quenching provides most of the energy given to translational degrees of freedom, and N_2(X), which acts as collisional partner for said quenching. At higher pressure, on the other hand, initially higher densities of electronically excited nitrogen and gas density provide a faster heating, which leads to a sharp increase in the V–T contribution.

Previous works on N_2 glow discharges have highlighted the importance of V–V processes in gas heating [50]. In the present work non-resonant V–V collisions are relevant during the first instants of the discharge, while their rate decreases significantly as the steady state is reached. The main difference with the cited work is the significantly higher pressure, gas temperature and electron density in the plasma core, which prevent the plateau in the bulk of VDF from forming, as shown in figure 12. The lower population of these intermediate vibrational levels therefore leads to a lower V–V contribution

to gas heating. This feature of the VDF can explain also the low contribution to gas heating given by collisions with nitrogen atoms, otherwise highlighted by Pintassilgo *et al* at lower pressures [50]. In fact, by comparing rate coefficients for V–T collisions on N_2 provided by Billing [35] and shown by Adamovich *et al* [33] with the rate coefficients shown by Guerra *et al* [24] for V–T collisions on N, it is clear that the former are significantly lower for gas temperatures below ∼1500 K and for intermediate levels (between 10 and 30). As gas temperature increases, rate coefficients for V–T (N) collisions with higher vibrational levels tend to quickly converge to $\sim 10^{-10}$ cm^3 s^{-1}, while the rate coefficients of V–T(N) collisions reach a maximum value of $\sim 10^{-12}$ cm^3 s^{-1}. This means that a plateau in the VDF can cause efficient gas heating due to V–T by N multi-quanta collisions if T_g is low enough, even with relatively low populations of N atoms in the discharge, which is the case in the work by Pintassilgo *et al* [50]. Even in the absence of the plateau, a recent combined experimental and modelling effort by Kelly *et al* [6] has shown that V–T (N) collisions are relevant for gas heating towards the end of a pulse in a MW discharge at 25 mbar: in this case the relatively low gas temperature (∼1500 K) combined with a relatively high N density (∼10% of the total gas density) are responsible for this behaviour.

In summary, in all the investigated conditions, most of the electron energy is converted into vibrational energy. The absolute value of the transferred energy depends on the input power density. As hypothesised before, reaction N3 and transport are responsible for vibrational cooling: they counterbalance the increasing available energy due to the increasing input power density, limiting vibrational excitation. The latter can be easily reduced by reducing the flow rate. The increase in creation rate of electronically excited N_2 at higher pressure, justified by the higher amount of available energy and the higher electron density, is the cause for fast gas heating and rupture of vibrational non-equilibrium, as quenching of N_2(A, B) is the main responsible for heating. This also explains the similar strong dependence on $P_{d,0}$ shown by n_e and T_g. Lower power density may therefore maintain higher degrees of non-equilibrium by reducing the fraction given to translational degrees of freedom through electronic excitation. The reduced n_e and N_2(A, B), however, can prove detrimental to dissociation, as the reaction rate for electron-impact dissociation and process N21 may be significantly reduced. This is investigated in the next section.

4.3. Dissociation and vibrational energy transport

The core of the discharge is composed mainly of molecules in the electronic ground state, while only ∼1% of the total density populates electronically excited states of N_2 and N, with the latter increasing with pressure and input power, as shown in figure 9. At fixed pressure, plasma length and plasma radius, the relative density of N depends strongly on power density. This is due to the fact that direct collisions with electrons provide a significant fraction of the total dissociation rate (figure 10); indirectly, electrons also drive the creation of excited molecules necessary for dissociation through reaction N21, which provides the most relevant contribution in

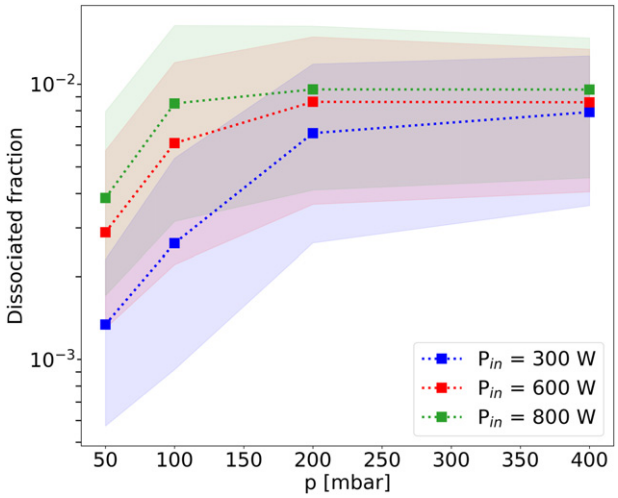

Figure 9. Dissociated fraction as a function of pressure for all experimental conditions, in the plasma core.

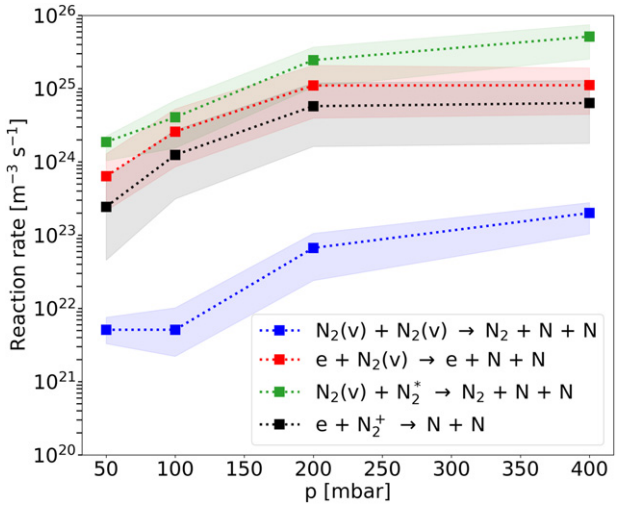

Figure 10. Rate coefficients of different dissociation mechanisms calculated from simulations as a function of pressure, at $P_{\text{in}} =$ 300 W, in the plasma core.

figure 10. The great variability of n_e under changes of $P_{d,0}$, already pointed out in figure 5, thus affects greatly the formation of N. However, if r_p and L are changed according to the values in table 1, the decrease in power density for the 200 mbar and 400 mbar cases is counterbalanced by the longer characteristic times for transport in both the radial and the axial direction, leading to an actual increase in dissociated fraction in the core. The longer residence time in the core may give N enough time to recombine, instead of being transported out. For the simulated conditions, the characteristic time for transport in the axial direction is between 1.5 and 6 ms, increasing with pressure and power. Despite the longer residence time, the number of atoms leaving the core per unit time and unit volume is always increasing with pressure, as the dissociation rate increases more steeply with p.

Note that the degree of dissociation found in the present work (between 0.001 and 0.01, according to figure 9) is 1

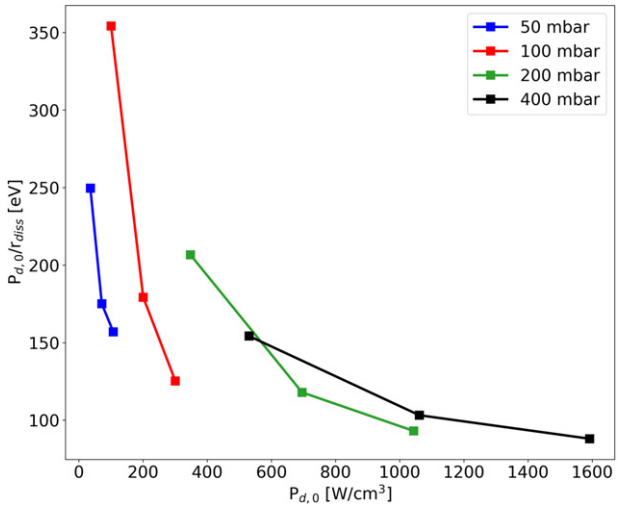

Figure 11. Energy cost per atom in the plasma core as a function of peak power density at different values of pressure, for $P_{\text{in}} = 300$ W. The three points for each pressure condition correspond to 0.5, 1 and 1.5 times the value of $P_{d,0}$ estimated from experiments.

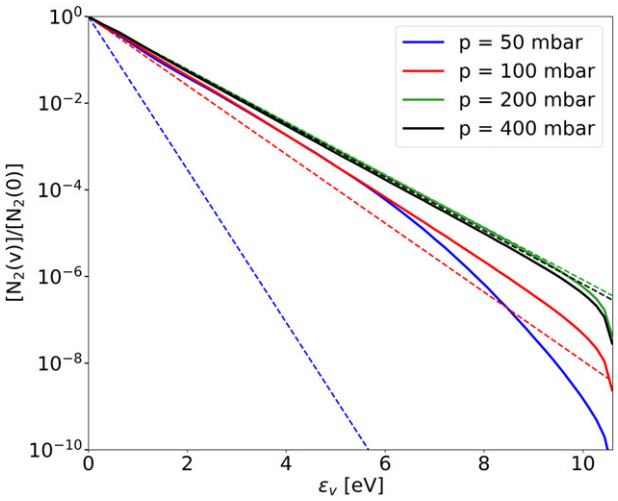

Figure 12. VDF at different pressures and $P_{\text{in}} = 300$ W. The dashed line (----) represents the Boltzmann distribution at T_g, in the plasma core.

to 2 orders of magnitude lower than the one estimated in previous papers [6, 13]. This can be explained by noting that the power density in those works reaches values at least 2 orders of magnitude higher than the ones under study here. This increased input power density results in higher E/n_{gas}, favouring electronic excitation, which in turn results in a higher electron density ($\sim 10^{20}$ m^{-3} in Kelly's work [6]), due to increased associative ionization (I1 and I2 in table 4) and electron impact ionization. The higher electron density enhances the rate of dissociative recombination (I11 and I12) and of electron-impact dissociation of $N_2(X, v)$, resulting in a higher dissociated fraction.

In order to evaluate the impact of vibrational excitation on dissociation, the amount of energy used to obtain 1 atom of nitrogen has been estimated as:

$$\epsilon_{\text{N}} = \frac{P_{d,0}}{r_{\text{N}}} \tag{35}$$

where r_{N} is the rate of production of N, calculated as the sum of all dissociation rates. Figure 11 shows the variation of this quantity with input power density for different pressures, considering the values of L and r_p obtained from the measurements at 300 W of input power. Looking at the data at constant pressure, increase in power density leads to a decrease in energy cost, due to the enhancement of reaction N21, caused both by the higher density of $N_2(A)$ and a higher vibrational temperature; this effect saturates at 400 mbar, as T_v is bound to T_g, which in turn is limited by transport and radiation losses. When power density is decreased, instead, the lower vibrational temperature and consequent lower population of the vibrational levels between 15 and 19 (between $\sim$4 eV and $\sim$5 eV) leads to an increased energy cost. Estimated energy costs per atom for thermal plasmas reported by Fridman [5] also show a decrease with increasing T_v, even though the investigated pressures are much lower than the ones taken into account in this work. The energy costs reported in the aforementioned work are, however, two orders of magnitude lower than the ones reported here. Those values are calculated as the sum of the energy necessary to heat the gas to a given temperature T_g and the reaction enthalpy is divided by the amount of produced atoms. By calculating the energy cost per atom as the ratio between the input power density and the total production rate of N, this work takes into account the additional energy that needs to be injected into the system to overcome losses due to heat dissipation at the wall and transport. Additionally, as previously discussed, only $\sim$30% of the injected power density results in gas heating, with the rest being transferred to vibrational degrees of freedom. The predicted energy necessary for gas heating is between $\sim$2 eV and $\sim$6 eV in the temperature range investigated in the present work, which in our system increases to values between $\sim$10 eV and $\sim$20 eV, considering that only one third of the energy is directed towards heating. This only makes up for part of the energy cost. The remainder is explained by the fact that nitrogen molecules are not only lost through dissociation, but can also be lost through ionization and transport, meaning that there is not a 100% selectivity towards dissociation, as assumed in [5].

Figure 11 also shows that, at similar values of input power density, the energy cost per atom decreases with decreasing pressure. As in these cases T_v does not change relevantly (figure 2), this is due to the higher degree of non-equilibrium achieved at lower pressure, which translates into a higher population in the vibrational energy region between 4 and 5 eV. This is even more evident when comparing the point at 50 mbar and 75 W cm^{-3} with the one at 100 mbar and 207 W cm^{-3}: despite the higher T_v reached at 100 mbar ($\sim$7200 K), the non-equilibrium maintained at 50 mbar counterbalances the effect of the lower T_v ($\sim$6800 K), allowing the energy cost per atom to be similar in the two cases. In fact, in these conditions, the VDF at 50 and 100 mbar clearly overlap in the region involved in reaction N21, as shown by figure 12.

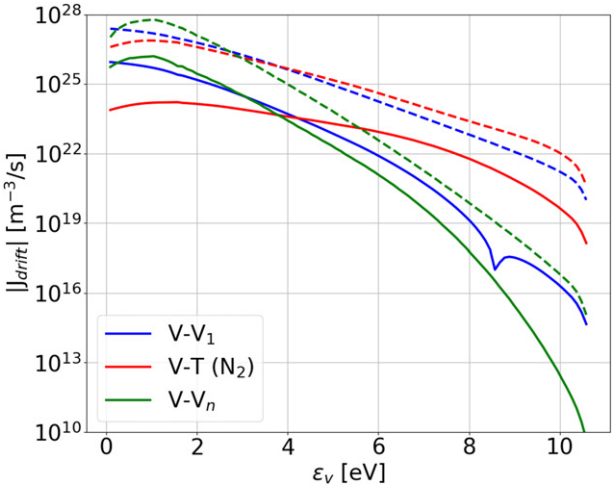

Figure 13. Drift component of the flux in energy space, as modelled with equation (7), for different processes at 50 mbar (solid line) and 400 mbar (dashed line), at $P_{\text{in}} = 300$ W.

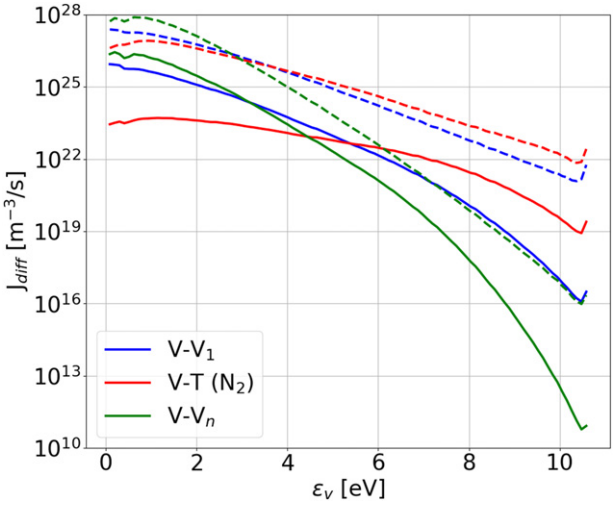

Figure 14. Diffusive component of the flux in energy space, as modelled with equation (7), for different processes at 50 mbar (solid line) and 400 mbar (dashed line), at $P_{\text{in}} = 300$ W.

The increased population of those levels with respect to a Boltzmann distribution is due to the lower strength of V–T relaxation at $T_g \sim 2800$ K, as shown by figures 13 and 14, where the magnitude of the drift (J_{drift}) and diffusive (J_{diff}) component of the flux in energy space in the modified FP equation (equation (7)) is plotted as a function of vibrational energy for the most relevant V–V and V–T processes; note that V–T collisions with atomic nitrogen have been omitted as their contribution is negligible. These quantities are defined as:

$$J_{\text{drift}}(\epsilon) = A(\epsilon) f(\epsilon) \tag{36}$$

$$J_{\text{diff}}(\epsilon) = -B(\epsilon) \frac{\mathrm{d}f(\epsilon)}{\mathrm{d}\epsilon}. \tag{37}$$

Note that figure 13 shows the absolute value of J_{drift}, as this last is always negative, meaning that molecules are drifting towards the lower energy side of the domain. A change in sign from negative to positive is seen only for V–V$_1$ process at 50 mbar (full blue line in figure 13) at around 8.5 eV (where a dip is visible): positive flux would lead to population of the tail of the distribution, but that flux is counterbalanced by the higher negative flux due to V–T relaxation. A lower V–T rate in this region would lead to higher population of the high energy levels and increased e–V dissociation.

The diffusion component of the flux is always positive, but shows a similar dependence on the vibrational energy: this means that the tendency to drift towards the low energy side of the domain is countered by a diffusive tendency to populate states with lower particle density. The increase at the far end of the energy domain is due to the increase in the derivative of $f(\epsilon)$ caused by dissociation; the drift component, instead, decreases, therefore leading to a dominant positive diffusive component, trying to repopulate the tail that is being depleted by dissociation.

Differently from the case at 400 mbar, the diffusive component of the flux for V–T relaxation at 50 mbar is lower than the drift one, meaning that the net flux in the region between 4 eV and 10 eV is negative: this is due to the fact that population of these levels is larger than the one expected for a Boltzmann distribution at T_g; this causes an imbalance between the probability of moving to higher levels and the probability of moving to lower levels due to V–T collisions, resulting in a negative drift. Since V–V$_1$ and V–V$_n$ fluxes are lower in this region, the population of these levels is determined by the source terms, in particular by e–V collisions.

In summary, non-equilibrium is beneficial for N_2 dissociation only if T_v is also high enough (above 6000 K). The non-equilibrium is achieved by keeping a low density of electronically excited states, so that excessive gas heating is prevented and V–T rate is low enough to allow a build-up of molecules in the vibrational states involved in reaction N21. This build-up is determined by e–V collisions, rather than vibrational ladder climbing due to V–V processes. Low energy cost per atom can be achieved at high pressure, due to the higher vibrational temperature, favouring reaction N21, hence allowing a higher yield, if the power density is increased. It should however be noted that simply increasing P_{in} does not lead to the desired effect in the set-up used for this study, as the increase in plasma volume causes $P_{d,0}$ to saturate as input power is increased.

5. Conclusions

In this work, N_2 continuous MW discharges in different conditions have been studied both via experiments and simulations to gain insights into N_2 vibrational excitation, gas heating and their impact on dissociation in the plasma core, for pressures varying from 50 to 400 mbar and input powers between 300 and 800 W.

A state-of-the-art 0D model of the plasma core, coupling the FP approach to vibrational kinetics with the solution of the particle balance equation, heat equation, vibrational energy equation and electron Boltzmann equation has been developed and employed for the first time. Treating vibrational kinetics via the FP formulation allows reduction of the computational

time by a factor 0.7 with respect to the STS approach; further increase of computational efficiency is required and may be achieved by optimizing drift and diffusion coefficient calculations. Insights into the transport of energy due to V–V and V–T processes has revealed the role of e–V collisions in maintaining the overpopulation of higher vibrational levels.

Comparison with experiments reveals a good agreement both qualitatively and quantitatively in terms of vibrational and gas temperature, and electron density. Electron temperature appears overestimated by simulations beyond the reasonable error associated with the input power density value, suggesting a shortcoming either of the chemistry set or of the 0D model. Nevertheless, detailed insight into energy exchange mechanisms at different regimes has been obtained from simulations results, pointing at the fast quenching of N_2(A, B) as the mechanisms causing gas heating and disruption of the non-equilibrium otherwise obtained at 50 mbar. Energy confinement into vibrational degrees of freedom is therefore achieved at 50 mbar thanks to the lower input power density, leading to lower electron density and therefore lower electronic excitation. Quenching of vibrational levels due to collisions with N atoms does not cause a relevant loss of vibrational energy.

Vibrational temperature has been shown to depend weakly on the input power density, due mainly to two phenomena. Firstly, axial transport of vibrationally excited molecules contributes to at least 20% of vibrational energy losses, acting as a cooling effect roughly independent from the input power density. Secondly, process N3 consumes up to 80% of the energy loaded into vibrations. Since it requires N_2(A) as collisional partner, it is enhanced by increasing power density, hence counterbalancing its effect on vibrational excitation.

Vibrational excitation has been shown to lower the energy cost for dissociation of N_2, which occurs mainly through collisions between vibrationally excited molecules and the electronically excited state N_2(A). Electron-impact dissociation of vibrationally excited molecules is also proved to be relevant, though the electron density and the value of E/n_{gas} achieved in the explored conditions (between 30 and 40 Td) are not high enough to make it the most relevant process.

Vibrationally-enhanced dissociation lowers the energy cost per atom, which reaches the lowest value at higher values of input power density, where T_v reaches ∼8000 K. For cases with similar values of vibrational temperature, higher values of T_v/T_g leads to a lower energy cost per atom. As discussed above, this occurs at low input power density values.

Nevertheless, estimated values of ϵ_{N}, the amount of energy used to obtain 1 atom of nitrogen, are two orders of magnitude higher than what predicted by Fridman [5]. This is explained by the presence of lower reaction selectivity towards dissociation than estimated in [5] and the presence of heat losses in the model presented in this work. The values predicted by Fridman are calculated assuming no energy losses from the system, while the simulations of this work take into account losses of energy due to both transport and wall dissipation of heat.

Space resolved simulations of the discharges may reveal a different scenario, as T_v/T_g has been shown to increase outside the core at pressures lower than 50 mbar [11]. This motivates a future upgrade of the simulation dimensionality.

Moreover, the input power density, which is only roughly estimated by experiments, plays a more relevant role in determining energy partitions in the MW discharge than pressure and input power alone. In fact, electron density, electronically excited species densities and ultimately gas temperature, which play relevant roles in the dissociation processes, are all strongly dependent on P_d. Increasing accuracy of the simulations therefore also relies on more accurate measurements of power density profiles.

Acknowledgments

This research received funding from the Netherlands Organization for Scientific Research (NWO) in the framework of the project ‘Insight into more efficient plasma conversion from vibrational energy diffusion modelling’ (OCENW.KLEIN.107). PV acknowledges support by Project LM2018097 funded by the Ministry of Education, Youth and Sports of the Czech Republic. PV also acknowledges support by the Portuguese FCT—Fundação para a Ciência e a Tecnologia, under Projects UIDB/50010/2020, UIDP/50010/2020 and PTDC/FIS-PLA/1616/2021 (PARADiSE).

Data availability statement

The data that support the findings of this study are available upon reasonable request from the authors.

ORCID iDs

P Viegas https://orcid.org/0000-0002-3820-3300
A W van de Steeg https://orcid.org/0000-0002-2976-7905
S Longo https://orcid.org/0000-0002-5038-7659
G J van Rooij https://orcid.org/0000-0003-4795-3274
P Diomede https://orcid.org/0000-0002-4523-3049

References

[1] Patil B, Wang Q, Hessel V and Lang J 2015 *Catal. Today* **256** 49–66
[2] Cherkasov N, Ibhadon A and Fitzpatrick P 2015 *Chem. Eng. Process.* **90** 24–33
[3] Bogaerts A and Neyts E C 2018 *ACS Energy Lett.* **3** 1013–27
[4] Kelly S and Bogaerts A 2021 *Joule* **5** 3006–30
[5] Fridman A 2008 *Plasma Chemistry* (Cambridge: Cambridge University Press)
[6] Kelly S, van de Steeg A, Hughes A, van Rooij G and Bogaerts A 2021 *Plasma Sources Sci. Technol.* **30** 055005
[7] Brovikova I N and Galiaskarov E G 2001 *High Temp.* **39** 809–14
[8] Guerra V, Tatarova E and Ferreira C 2002 *Vacuum* **69** 171–6
[9] Guerra V, Galiaskarov E and Loureiro J 2003 *Chem. Phys. Lett.* **371** 576–81
[10] Volynets A, Lopaev D, Rakhimova T, Chukalovsky A, Mankelevich Y A, Popov N, Zotovich A and Rakhimov A 2018 *J. Phys. D: Appl. Phys.* **51** 364002

[11] Gatti N, Ponduri S, Peeters F, Van Den Bekerom D, Minea T, Tosi P, Van De Sanden M and Van Rooij G 2018 *Plasma Sources Sci. Technol.* **27** 055006

[12] Van Alphen S, Vermeiren V, Butterworth T, van den Bekerom D C M, Van Rooij G J and Bogaerts A 2019 *J. Phys. Chem.* C **124** 1765–79

[13] van de Steeg A, Butterworth T, van den Bekerom D, Silva A, van de Sanden M and van Rooij G 2020 *Plasma Sources Sci. Technol.* **29** 115001

[14] Rusanov V, Fridman A and Sholin G 1979 *Zh. Tekh. Fiz.* **24** 318–22

[15] Macheret S, Rusanov V and Fridman A 1984 *Sov. Phys. Dokl.* **29** 222

[16] Fridman A and Kennedy L A 2004 *Plasma Physics and Engineering* (Boca Raton, FL: CRC Press)

[17] Capitelli M 2012 *Nonequilibrium Vibrational Kinetics* vol 39 (Berlin: Springer)

[18] Diomede P, Van De Sanden M C and Longo S 2017 *J. Phys. Chem.* C **121** 19568–76

[19] Diomede P, van de Sanden M C and Longo S 2018 *J. Phys. Chem.* A **122** 7918–23

[20] Viegas P, van de Sanden M C, Longo S and Diomede P 2019 *J. Phys. Chem.* C **123** 22823–31

[21] Altin M, Vialetto L, Longo S, Viegas P and Diomede P A modified Fokker–Planck approach for a complete description of vibrational kinetics in a N_2 plasma chemistry model J. Phys. Chem. C (submitted)

[22] Vialetto L, van de Steeg A, Viegas P, Longo S, Van Rooij G J, Van de Sanden R, van Dijk J and Diomede P 2022 *Plasma Sources Sci. Technol.* **31** 055005

[23] Viegas P, Vialetto L, van de Steeg A W, Wolf A, Bongers W A, van Rooij G J, van de Sanden M, Diomede P and Peeters F 2021 *Plasma Sources Sci. Technol.* **30** 065022

[24] Guerra V, Tejero-del Caz A, Pintassilgo C D and Alves L L 2019 *Plasma Sources Sci. Technol.* **28** 073001

[25] den Harder N *et al* 2017 *Plasma Process. Polym.* **14** 1600120

[26] van de Steeg A W, Vialetto L, Silva A, Peeters F, van den Bekerom D C, Gatti N, Diomede P, Van de Sanden M and van Rooij G J 2021 *Opt. Lett.* **46** 2172–5

[27] van de Steeg A, Vialetto L, Silva A S d, Viegas P, Diomede P, van de Sanden M and van Rooij G 2022 *J. Phys. Chem. Lett.* **13** 1203–8

[28] Van de Sanden M and Van der Mullen J 2002 *J. Phys. D: Appl. Phys.* **35** 1381

[29] Carbone E, Hübner S, Palomares J and Van Der Mullen J 2012 *J. Phys. D: Appl. Phys.* **45** 345203

[30] Viegas P, Vialetto L, Wolf A, Peeters F, Groen P, Righart T, Bongers W, van de Sanden M and Diomede P 2020 *Plasma Sources Sci. Technol.* **29** 105014

[31] Guerra V, Sá P and Loureiro J 2004 *Eur. Phys. J. Appl. Phys.* **28** 125–52

[32] Adamovich I V 2001 *AIAA J.* **39** 1916–25

[33] Adamovich I V, Macheret S O, Rich J W and Treanor C E 1998 *J. Thermophys. Heat Transfer* **12** 57–65

[34] Ahn T, Adamovich I V and Lempert W R 2004 *Chem. Phys.* **298** 233–40

[35] Billing G D and Fisher E 1979 *Chem. Phys.* **43** 395–401

[36] Da Silva M L, Guerra V and Loureiro J 2007 *J. Thermophys. Heat Transfer* **21** 40–9

[37] IST-Lisbon database www.lxcat.net (accessed 29 November 2020).

[38] Bacri J and Medani A 1982 *Physica B+C* **112** 101–18

[39] Wang Y, Zatsarinny O and Bartschat K 2014 *Phys. Rev.* A **89** 062714

[40] Zipf E and McLaughlin R 1978 *Planet. Space Sci.* **26** 449–62

[41] Sakiyama Y and Graves D B 2007 *J. Appl. Phys.* **101** 073306

[42] Grubert G, Becker M and Loffhagen D 2009 *Phys. Rev.* E **80** 036405

[43] Hirschfelder J and Curtiss C 1948 Theory of propagation of flames: I. General equations *Symp. on Combustion and Flame, and Explosion Phenomena* vol 3 (Elsevier) pp 121–7

[44] Hirschfelder J O, Curtiss C F and Bird R B 1964 *Molecular Theory of Gases and Liquids* (New York: Wiley)

[45] Yaney P P and Parish J W 1999 Studies of surface deactivation of vibrationally-excited homonuclear molecules in gaseous discharge media using coherent anti-Stokes Raman spectroscopy (CARS) *Technical Report* (OH: Dayton Univ.)

[46] Marinov D, Lopatik D, Guaitella O, Hübner M, Ionikh Y, Röpcke J and Rousseau A 2012 *J. Phys. D: Appl. Phys.* **45** 175201

[47] Ellis H W, Pai R Y, McDaniel E W, Mason E A and Viehland L A 1976 *At. Data Nucl. Data Tables* **17** 113–51

[48] Hagelaar G and Pitchford L C 2005 *Plasma Sources Sci. Technol.* **14** 722

[49] Pintassilgo C, Guerra V, Guaitella O and Rousseau A 2014 *Plasma Sources Sci. Technol.* **23** 025006

[50] Pintassilgo C D and Guerra V 2017 *Plasma Sources Sci. Technol.* **26** 055001

[51] Chase M W 1998 *NIST-JANAF Themochemical Tables NIST-JANAF Themochemical Tables* vol 9) (Woodbury, New York: American Institute of Physics) 4th edn J. Phys. Chem. Ref. Data

[52] Kutasi K, Pintassilgo C, Coelho P and Loureiro J 2006 *J. Phys. D: Appl. Phys.* **39** 3978

[53] Booth J-P *et al* 2019 *Plasma Sources Sci. Technol.* **28** 055005

[54] Pintassilgo C D and Guerra V 2016 *J. Phys. Chem.* C **120** 21201

[55] Shkurenkov I and Adamovich I V 2016 *Plasma Sources Sci. Technol.* **25** 015021

[56] Lepikhin N, Popov N and Starikovskaia S 2018 *Plasma Sources Sci. Technol.* **27** 055005

[57] Mintoussov E, Pendleton S, Gerbault F, Popov N and Starikovskaia S 2011 *J. Phys. D: Appl. Phys.* **44** 285202

[58] Aubrecht V and Bartlova M 2008 Radiation transfer in thermal plasmas of air, N_2 and CO_2 *2008 17th Int. Conf. on Gas Discharges and Their Applications* (Piscataway, NJ: IEEE) pp 393–6

[59] Patankar S V 2018 *Numerical Heat Transfer and Fluid Flow* (Boca Raton, FL: CRC Press)